JCB Journal of Cell Biology

ARTICLE

Vimentin filament transport and organization revealed by single-particle tracking and 3D FIB-SEM

Bhuvanasundar Renganathan[1]*, Andrew S. Moore[2]*, Wei-Hong Yeo[3], Alyson Petruncio[2], David Ackerman[2], Aubrey V. Weigel[2], The CellMap Team[2], H. Amalia Pasolli[4], C. Shan Xu[5], Gleb Shtengel[2], Harald F. Hess[2], Anna S. Serpinskaya[1], Hao F. Zhang[3], Jennifer Lippincott-Schwartz[2], and Vladimir I. Gelfand[1]

Vimentin intermediate filaments (VIFs) form complex, tightly packed networks; due to this density, traditional imaging approaches cannot discern single-filament behavior. To address this, we developed and validated a sparse vimentin-SunTag labeling strategy, enabling single-particle tracking of individual VIFs and providing a sensitive, unbiased, and quantitative method for measuring global VIF motility. Using this approach, we define the steady-state VIF motility rate, showing a constant ∼8% of VIFs undergo directed microtubule-based motion irrespective of subcellular location or local filament density. Significantly, our single-particle tracking approach revealed uncorrelated motion of individual VIFs within bundles, an observation seemingly at odds with conventional models of tightly cross-linked bundles. To address this, we acquired high-resolution focused ion beam scanning electron microscopy volumes of vitreously frozen cells and reconstructed three-dimensional VIF bundles, finding that they form only loosely organized, semi-coherent structures from which single VIFs frequently emerge to locally engage neighboring microtubules. Overall, this work demonstrates single VIF dynamics and organization in the cellular milieu for the first time.

Introduction

Intermediate filaments (IFs) comprise a large class of cytoskeletal polymers encoded by a family of over 70 distinct genes (Szeverenyi et al., 2008). IFs form extended, semiflexible fibers with characteristic ∼10–12-nm widths (Steinert et al., 1985; Eibauer et al., 2024; Ishikawa et al., 1968). Type III IFs include a closely related subset of these proteins, which form mature assemblies within the cytoplasm and display striking cell-type specificity (Herrmann et al., 2007; Redmond and Coulombe, 2021; Omary et al., 2004). Vimentin, perhaps the best studied type III IF protein, is canonically expressed in mesenchymal cells such as fibroblasts and forms complex, multifunctional networks (Lowery et al., 2015).

Due to their abundance, unique distribution, and biophysical properties, vimentin intermediate filaments (VIFs) are ideally suited to organize cytoplasmic space (Vikstrom et al., 1992; Hu et al., 2019; Pogoda and Janmey, 2023). VIFs interact with actin and microtubules (MTs), fostering cytoskeletal crosstalk required to adapt cell shape to ongoing cellular needs (Lynch et al., 2013; Kim and Coulombe, 2007; Pallari and Eriksson, 2006). VIFs also associate with subcellular organelles, including Golgi membranes (Vitali et al., 2023), mitochondria (Nekrasova et al., 2011), and the nuclear envelope (Patteson et al., 2019; Pogoda et al., 2022), to influence membrane structure, dynamics, and subcellular positioning (Lowery et al., 2015; Chang et al., 2009). Accordingly, pathological conditions that disrupt IF structure or dynamics are often marked by disordered subcellular organization (Renganathan et al., 2023; Coelho-Rato et al., 2024; Szeverenyi et al., 2008; Bomont, 2021).

VIF subcellular distribution is notably nonuniform, exhibiting a radial gradient of filament density. In the perinuclear region, densely tangled VIF bundles crisscross the cytoplasm, while at the cell periphery, sparser and simpler filament arrangements predominate. When first characterized by early immunocytochemistry studies, this unique organization of VIF networks was presumed to reflect a largely static, immobile character (Starger et al., 1978; Franke et al., 1978). This interpretation was revised upon the development of live fluorescence microscopy techniques that allowed for time-lapse movies of fluorescent protein–tagged vimentin in living cells (Ho et al., 1998; Prahlad et al., 1998; Yoon

---

[1]Department of Cell and Developmental Biology, Feinberg School of Medicine, Northwestern University, Chicago, IL, USA; [2]Janelia Research Campus, Howard Hughes Medical Institute, Ashburn, VA, USA; [3]Department of Biomedical Engineering, Northwestern University, Evanston, IL, USA; [4]Electron Microscopy Resource Center, Rockefeller University, New York, NY, USA; [5]Department of Cellular and Molecular Physiology, Yale School of Medicine, Yale University, New Haven, CT, USA.

Members of The CellMap Team: Aubrey V. Weigel, Marley Bryant, Grace Park, Alyson Petruncio, Alannah Post, Jacquelyn Price, Diana Ramirez, Jeff Rhoades, Rebecca Vorimo, Yurii Zubov

*B. Renganathan and A.S. Moore contributed equally to this paper. Correspondence to Vladimir I. Gelfand: vgelfand@northwestern.edu.

Rockefeller University Press https://doi.org/10.1083/jcb.202406054
J. Cell Biol. 2025 Vol. 224 No. 4 e202406054

et al., 1998). Live imaging and the use of techniques such as fluorescence recovery after photobleaching (FRAP) and targeted photoactivation/photoconversion demonstrated that vimentin filaments move along MTs (Robert et al., 2016). VIF motility was subsequently shown to play key roles in cell migration and wound healing (Eckes et al., 2000; Cheng et al., 2016; Gan et al., 2016).

Though these techniques were invaluable in identifying and defining the ensemble behavior of the vimentin cytoskeleton, they are limited in their ability to report on the motility of single filaments within the broader VIF network. As single filaments are ~10–12 nm in diameter, it is impossible in conventional light microscopy movies to determine whether elongated, threadlike vimentin structures are true single filaments or bundled arrays. In the perinuclear region, where vimentin filament density is the highest, the problem is further compounded. To investigate the behavior of single VIFs, the field has largely favored in vitro reconstitution assays, in which VIFs are assembled in a cell-free system and assayed by total internal reflection fluorescence microscopy (Winheim et al., 2011). These assays have helped to define fundamental VIF properties, including their dynamics (Lazarides, 1982; Brennich et al., 2014; Portet et al., 2009), mechanics (Janmey et al., 1991), their interactions with other cytoskeletal polymers (Shen et al., 2021; Schaedel et al., 2021), and even their propensity to form multifilament bundles (Wu et al., 2020). However, these VIF properties are underexplored in their native environment, in intact cells.

In this study, we used single-particle tracking (SPT) and volume electron microscopy (EM) reconstruction to define the motion and organization of VIFs in cultured cells. First, we developed a novel VIF reporter based on the SunTag labeling system. Through tuning the expression of our reporter, we achieved a labeling density that enabled unambiguous long-term tracking of single VIFs throughout all regions of the cytoplasm, including the dense and notoriously irresolvable perinuclear vimentin cytoskeleton. We confirmed the specificity of our probe using immunofluorescence and platinum replica electron microscopy (PREM) and established the sensitivity of our workflow by simultaneously tracking thousands of SunTag particles in a single cell and quantifying VIF motility changes in response to previously validated modulators of vimentin dynamics. In correlative experiments with a co-expressed ensemble vimentin marker, our single-filament reporter revealed extensive bidirectional VIF transport in regions that appeared static and tightly bundled. This observation challenged our assumption of tightly cross-linked VIF bundles that behave as a rigid unit, instead of hinting at a model in which individual VIFs dynamically enter and exit bundles. To investigate the precise nanoscale organization of vimentin filaments in their native environment, we obtained isotropic focused ion beam scanning electron microscopy (FIB-SEM) volumes of cultured cells and reconstructed VIFs and MTs in either the highly bundled perinuclear region or the sparse cell periphery.

Results

Vimentin-SunTag incorporates into endogenous VIFs

To enable high-speed tracking of individual vimentin filaments within dense networks, we sought to develop a system for ultrabright, low-density labeling. To accomplish this, we created a single-molecule reporter using the two-component SunTag system. Specifically, we designed a fusion protein of human vimentin linked to a synthetic scaffold harboring 24 copies of GCN4 peptide epitopes (Tanenbaum et al., 2014). This scaffold is co-expressed with an anti-GCN4 single-chain variable fragment of antibody (scFv) fused to superfolded GFP (sfGFP) (see Materials and methods for details). Upon expression, the scFv-GCN4-sfGFP binds to the GCN4 epitopes on the SunTag scaffold, placing multiple copies of GFP in a single spot and significantly amplifying the fluorescence signal of the tagged vimentin monomer (Fig. 1 A).

Under standard overexpression conditions, this system would drive ultrabright, dense labeling of the entire vimentin network, making it impossible to resolve individual filaments. However, by dramatically limiting vimentin-SunTag expression levels through a reduced-efficiency promoter, we achieved a labeling density of less than one tagged vimentin molecule per filament. At this low density, the motion of each SunTag spot could be reasonably assumed to correspond to the motion of the single VIF in which it is incorporated. Thus, SPT of bright, stable, and resolvable SunTag spots could be used to infer single VIF dynamics, even in a dense, traditionally irresolvable region of the vimentin cytoskeleton (Fig. 1 A).

We co-transfected retinal pigment epithelial (RPE) cells with scFv-GCN4-sfGFP and vimentin-SunTag under the control of a reduced-efficiency CMV100 promoter. After 24 h, we observed bright fluorescent spots sparsely distributed throughout the cytoplasm at a density of 4.35 ± 0.6 spots per μm^2 (mean ± SD). We noted modest variation in mean particle intensity (Fig. S1 A), consistent with baseline variability in scFv-GCN4-sfGFP loading onto GCN4 epitope arrays. At this low labeling density, individual SunTag spots were well spaced and easily resolvable with a mean nearest neighbor distance (NND) of 814 ± 670 nm (mean ± SD; Fig. S1, B and C). Together, these observations suggest that we achieved sufficiently low vimentin-SunTag labeling density to enable unambiguous localization of single spots, an essential requirement for subsequent SPT.

To validate the specificity of our tool, we analyzed the spatial relationship between sparse SunTag puncta and a conventional ensemble vimentin reporter. We observed unambiguous colocalization between vimentin-SunTag spots and co-expressed vimentin-mCherry, confirming that our probe was specifically incorporated into vimentin filaments (Fig. 1, B and C). Furthermore, we determined that the local concentration of SunTag particles within the cytoplasm was proportional to the density of underlying VIFs, as demonstrated by a strong spatial correlation between the Vimentin-SunTag particle count and the integrated density of a co-expressed vimentin-mCherry ensemble reporter (Fig. S1, D–F). Finally, we used immunostaining to confirm that the organization of endogenous vimentin was not altered upon the expression of Vimentin-SunTag (Fig. S2, A–C).

While these experiments demonstrate that our sparse-labeled probe broadly co-distributes with vimentin, we still sought to validate that the SunTag-fused vimentin monomer was specifically and stably integrating into mature, polymerized VIFs. To test this, we treated cells with 0.5% Triton X-100, a procedure that extracts soluble cytoplasmic structures but does not affect

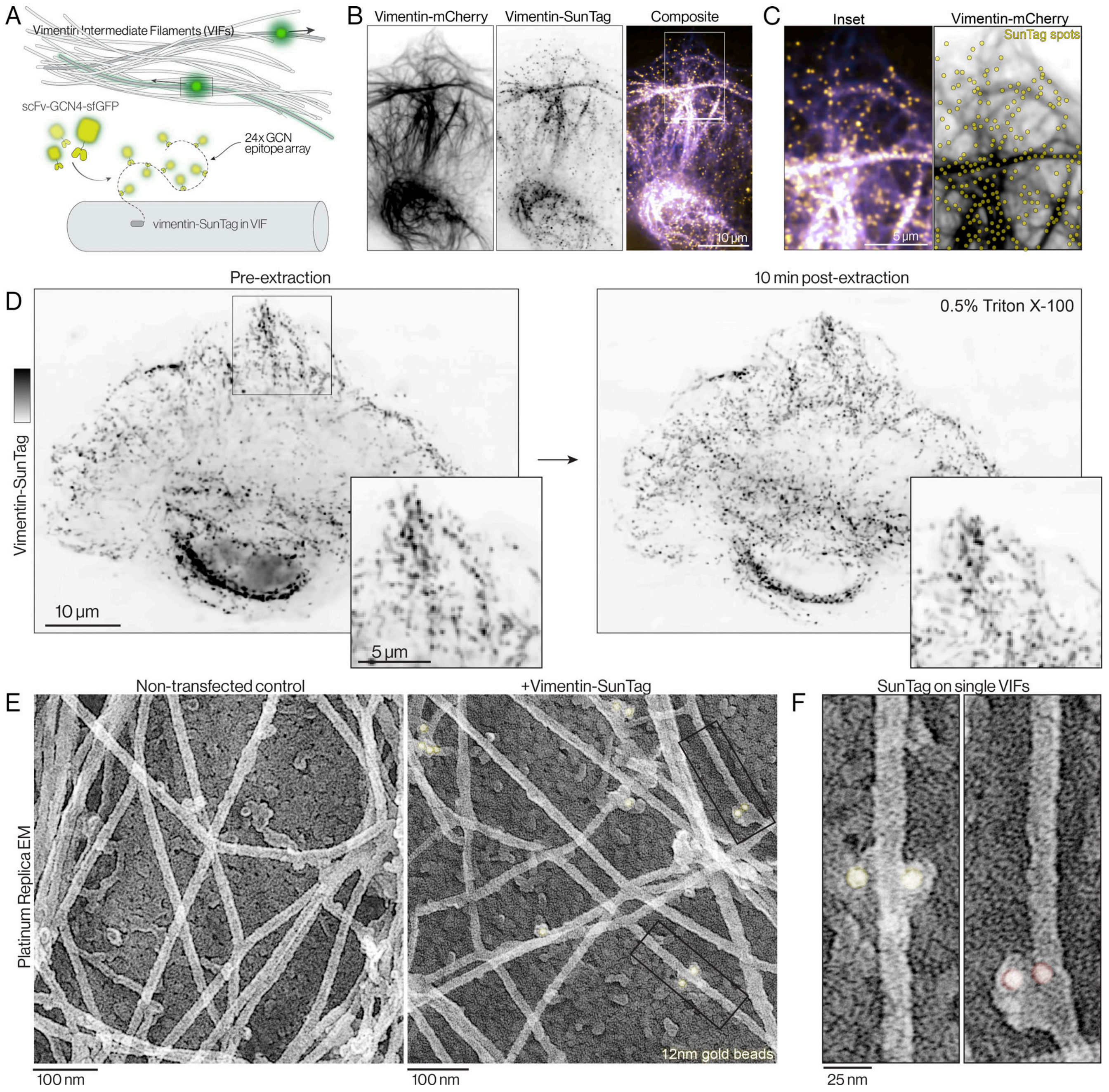

Figure 1. **Vimentin-SunTag sparse labeling of endogenous VIFs. (A)** Schematic of the vimentin-SunTag system design. **(B)** Co-expression of the ensemble vimentin reporter vimentin-mCherry (magenta in overlay) and sparse-labeled vimentin-SunTag (yellow in overlay), reused in Fig. S1 D. **(C)** Inset of the merged image from B (left) with localized SunTag particles overlaid. **(D)** Micrograph of RPE expressing sparse vimentin-SunTag before (left) or 10 min after (right) permeabilization/extraction with 0.5% Triton X-100. **(E)** PREM micrographs of a nontransfected RPE (left) or a vimentin-SunTag–expressing RPE (right). 12-nm gold beads affixed to anti-GFP antibodies are pseudocolored yellow. **(F)** Insets of single VIFs from E with gold-labeled vimentin-SunTag particles.

mature VIFs (Herrmann and Aebi, 2004; Starger et al., 1978; Nebl et al., 2002). If the vimentin-SunTag probe were integrated into mature filaments, we would expect little to no change in spot distribution upon detergent-mediated plasma membrane permeabilization. However, if tagged vimentin monomers were instead trapped in lower order assembly states or superficially bound to the surface of mature VIFs, we would expect a significant loss of spots upon cytoplasmic extraction. Notably, direct microscopic observation of Triton extraction in live cells did not reveal any appreciable decrease in the SunTag particle (Fig. 1 D), supporting the interpretation that the tagged monomers are appropriately incorporated into mature, polymerized vimentin.

To further validate that vimentin-SunTag is accurately targeted to single VIFs, we turned to PREM, a high-resolution imaging technique that enables detailed mapping of cytoskeletal structures at the filament level. Control and vimentin-SunTag–expressing RPE cells were extracted with 1% Triton X-100 for 5 min and subsequently fixed in 2% glutaraldehyde. To unambiguously identify SunTag particles, we labeled the fixed samples with a rabbit anti-GFP primary antibody followed by a 12-nm colloidal gold–conjugated anti-rabbit secondary antibody. Samples then underwent standard PREM processing, before final transmission EM images were collected. As anticipated, control cells that had not been transfected with vimentin-SunTag exhibited no visible gold particles (Fig. 1 E). In contrast, the vimentin-SunTag–transfected cells displayed clear 12-nm electron-dense particles associated with individual VIFs, consistent with the size of the colloidal gold particles (Fig. 1, E and F). VIF organization appeared comparable between control and sparse vimentin-SunTag expressors, indicating that the structure of endogenous VIFs was not disturbed by our reporter's expression.

Together, our light and EM data support the conclusion that SunTag-labeled vimentin monomers integrate into mature, endogenous VIFs and do not inhibit normal filament structure or organization. Having validated the specificity of our probe for single VIFs, we next turned our attention to the dynamics of SunTag spots in live cells to investigate the baseline motility of single VIFs.

SPT of vimentin-SunTag puncta reveals baseline VIF dynamics

To investigate the motion of individual VIFs, we transfected RPE cells with CMV100.vimentin-SunTag and captured 1-min movies of live cells at a 2-Hz acquisition rate. Under these sparse labeling conditions, we noted robust baseline vimentin-SunTag motion across all regions of the cytoplasm (Fig. 2 A and Video 1). Individual VIFs marked by SunTag spots appeared locally noncorrelated in their motion, and we observed a spectrum of distinct transport behaviors, including long-range directed motion, bidirectional transport, and stationary particles.

In comparison, cells expressing vimentin-SunTag under the control of a full-length CMV promoter displayed substantially higher ectopic expression, resulting in dense, at times nearly uniform filament labeling (Fig. S2 D and Video 2). While increased vimentin-SunTag label density did not affect the overall organization of the vimentin cytoskeleton, it did confound efforts to accurately identify single SunTag spots, thus precluding meaningful trajectory analysis. Notably, under this high expression condition, we frequently observed co-transport of spatially aligned vimentin-SunTag spots with constant relative spacing, a pattern consistent with multiple vimentin-SunTag integrations within a single motile filament (Fig. S2, E and F).

To rigorously quantify the dynamics of individual SunTag-labeled VIFs, we employed an automated SPT workflow. In brief, movies were processed with a B-spline wavelet filter, after which SunTag spots were identified using local intensity maxima and Gaussian fitting to achieve subpixel localization. This automated procedure, implemented using ThunderSTORM (Ovesný et al., 2014), provided spatial coordinates, intensity, size, and localization uncertainty for all detected particles in each frame of the analyzed movie. Localized SunTag particles were then linked across frames using the linear assignment problem (LAP) tracker (Jaqaman et al., 2008), and trajectories were subsequently filtered and processed for downstream analyses.

Initial inspection of the computed vimentin-SunTag trajectories revealed a marked heterogeneity in VIF track organization. Over each 60-s movie, we computed hundreds of individual trajectories in all parts of the cytoplasm with a wide distribution of track lengths (Fig. 2 B and Fig. S3 A). Due to the photostability of the SunTag array and our sparse labeling regime, we were able to reconstruct long trajectories that offered unique insights into the dynamic behavior of single VIFs over time (Fig. 2 C). In these trajectories, we observed complex motility patterns, including examples of directed anterograde and retrograde transport, bidirectional motility, unidirectional transport punctuated by subdiffusive pausing behaviors, and stationary particles (Fig. 2, C–E). While these dynamic VIF behaviors were often qualitatively apparent, many of the longer trajectories displayed a complex mix of different motility states. With the proliferation of SPT use within cell biology, there has been a wellspring of both conventional and AI methodologies to analyze trajectories and quantify distinct motility states (Simon et al., 2024, https://doi.org/10.1038/s43586-024-00341-3). Here, we used a 20-frame sliding window mean squared displacement (MSD) analysis to classify individual steps within trajectories by local alpha values (Fig. 2, F and G; and Fig. S3, B and C; see Materials and methods for details). This approach allowed us to more precisely identify segments that displayed confined subdiffusive behavior or directed superdiffusive motion (Fig. 2, F and G). The subtrajectory motility analyses enabled us to better characterize the complex behavior of specific filaments over time, identifying state switching events and other subtrajectory features that might not be appreciated with traditional edge or track analyses. However, this approach is heavily dependent on the size of the sliding window used for the MSD and is not suitable for analysis of the many shorter trajectories within our dataset (Fig. S3 D).

Shorter trajectories, curtailed by boundary effects, out-of-plane movement, or linkage failures, were comparatively less informative, capturing only brief snapshots of single VIFs over a few seconds and offering limited insight into their long-term motility. However, in aggregate, these shorter tracks contributed valuable data for characterizing the baseline fractional motility of the VIF cytoskeleton as a whole. To ensure a fair comparison, we standardized trajectories to 30 frames by filtering out those too short to be informative (<30 frames) and subdividing longer ones into nonoverlapping 30-frame (15-s) segments. We then classified the standardized trajectories as motile or immotile, based on whether their maximum displacement exceeded 1 µm (Fig. 2 H). In doing so, we could then perform detailed analyses on short trajectories sampled across the entire cell, allowing us to characterize global, steady-state VIF motility, an approach not possible using traditional methods such as FRAP. Using this approach, we found that ∼8–10% of all trajectories were classified as motile at any given time, providing the first baseline metric of global VIF fractional motility (Fig. 2 H; and Fig. S3, E and F).

Next, we compared track-level features between the motile and immotile groups. We observed that motile trajectories exhibited significantly higher maximum speeds, decreased mean direction change between steps, and substantially increased directionality ratio, confirming that our maximum displacement binning strategy was effectively capturing broad motility differences between the groups (Fig. S3, G–I). To gain deeper insights into the motion characteristics of each class, we performed lag-based analyses including MSD and velocity autocorrelation for time lags of up to 15 frames (Fig. 2 I). The MSD analysis

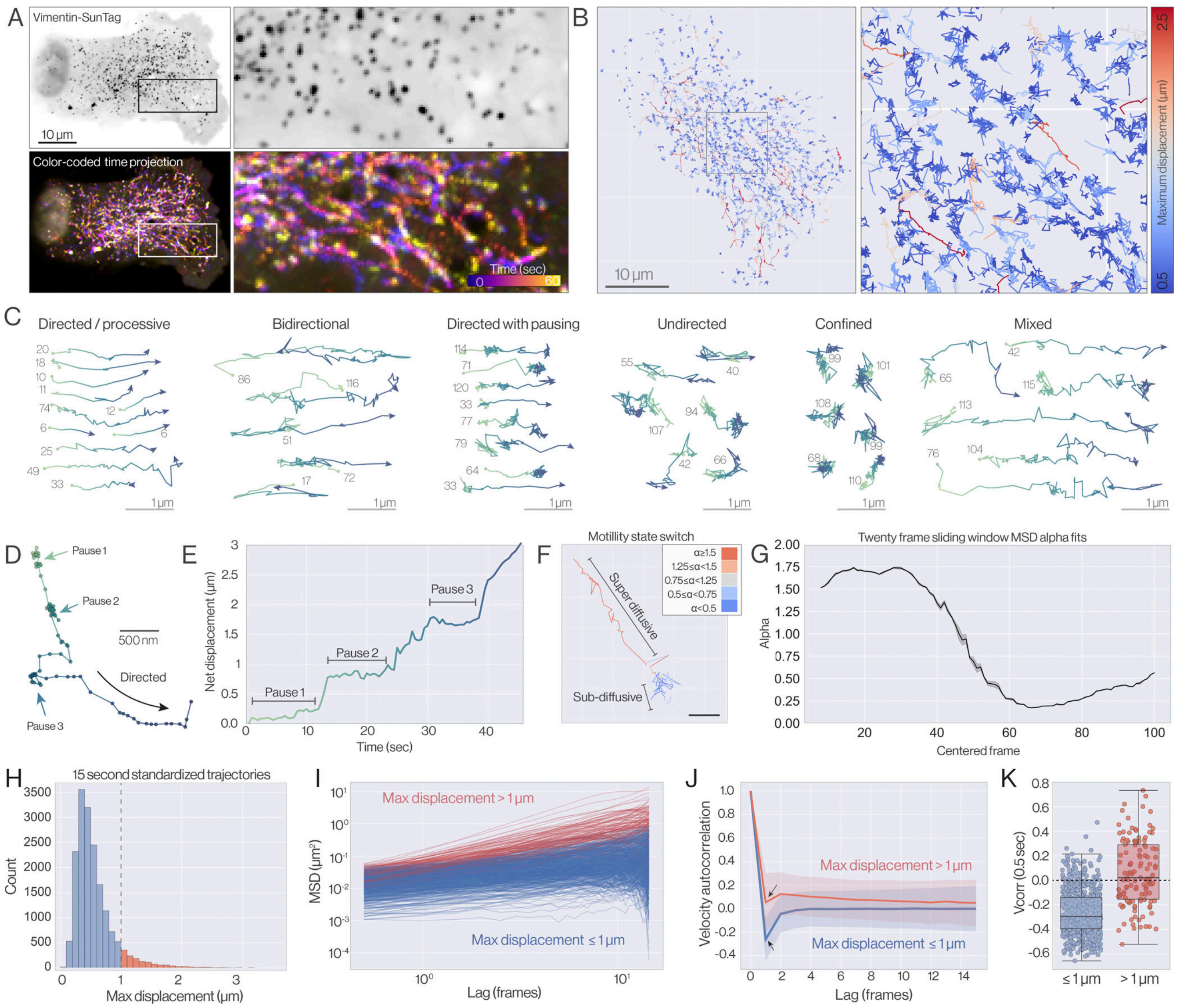

Figure 2. **SPT reveals complex VIF motility. (A)** (Top) Sparse SunTag labeling of the vimentin cytoskeleton in an RPE cell. (Bottom) Pseudocolored maximum intensity time projection of vimentin-SunTag puncta over 60 s. **(B)** SPT trajectories of vimentin-SunTag spots in a single cell over 1 min. Trajectories have been color-coded based on maximum displacement. The magnified inset is shown at right. **(C)** Representative vimentin-SunTag trajectories grouped by motile behavior. Numbers indicate track duration (in frames), dots indicate track starting points, edges are colorized by relative track position, and arrowheads indicate final track positions. **(D)** Representative vimentin-SunTag trajectory with multiple pausing events indicated by arrows. **(E)** Net displacement of the trajectory in E over time. Pausing events can be detected as extended durations with negligible changes in net displacement. **(F)** Representative vimentin-SunTag trajectory color-coded by the alpha value derived from sliding window MSD analysis (20 frame window width). **(G)** Alpha values for each 20-frame window centered at the indicated frame. **(H)** Frequency distribution of maximum displacements for standardized, 30-frame vimentin-SunTag trajectories indicating a cutoff used for immotile (<1 µm, blue) or motile (>1 µm, red) classification. *N* = 884 trajectories from the representative cell in B. **(I)** Distribution of directionality ratios for trajectories in each motility group. **(J)** MSD analysis of each motility group displayed on log–log axes. **(K)** Velocity autocorrelation at the first lag (0.5 s) for each motility group.

revealed that a greater proportion of trajectories in the motile class displayed superdiffusive behavior over the analyzed timescales, characteristic of active transport mechanisms driven by molecular motors. Conversely, tracks in the immotile class predominantly displayed subdiffusive motility assessed by MSD alpha fitting and stronger negative velocity autocorrelation peak at the first lag, suggestive of confinement or hindered diffusion, potentially due to anchoring to other cytoskeletal elements (Fig. 2, J and K).

By analyzing these track-level features and motion characteristics, we demonstrate that our vimentin-SunTag tool provides a validated, sensitive, and quantitative method for capturing the dynamic behaviors of individual VIFs while simultaneously assaying global vimentin motility rates across the entire cell.

VIF fractional motility is equivalent across perinuclear and peripheral subcellular regions

Given that the localization probability of vimentin-SunTag particles strongly correlates with local vimentin density (Fig. S1, D and E), we reasoned that we could infer relative rates of VIF motion in the sparse periphery versus the dense juxtanuclear region by simply analyzing fractional SunTag motility at different radial positions. We hypothesized that vimentin-SunTag would be mobile in the cell periphery, but comparatively confined within the dense, perinuclear region due to tight bundling.

To begin, we computed the initial radial position of all trajectories in our dataset. To account for variability in cell circularity/aspect ratio, we chose two complementary metrics of radial position: distance from the cell periphery, in which positions reflect simple Euclidean distances from the cell boundary, or normalized radial position, wherein tracks were assigned a value between 0 and 1, with 0 corresponding to the nuclear envelope and a value of 1 indicating the cell border (Fig. 3 A and Fig. S4, A–C; see Materials and methods for details). Next, using our track binning approach based on maximum displacement over 15 s, we again sorted all trajectories into two classes: motile (>1 µm max displacement) or immotile (max displacement ≤1 µm). Finally, we calculated the radial position and maximum displacement of trajectories from each class and visualized the resulting distributions as heatmaps (Fig. 3, B and C). Trajectories from both immotile and motile classes were observed throughout the cytoplasm, spanning both perinuclear (radial position <0.4) and peripheral (radial position >0.6) regions. While immotile trajectories were slightly more abundant near the juxtanuclear region, motile trajectories were not confined to the periphery, as one might expect given the denser bundling of VIFs near the nucleus. Instead, we observed directed motion across all radial positions, indicating that the cytoplasmic organization of vimentin does not preclude motility within dense, perinuclear regions (Video 3).

Vimentin-SunTag reports VIF motility changes in response to known VIF modulators

Having confirmed the specificity and sensitivity of vimentin-SunTag as a reporter for steady-state single VIF dynamics, we next explored whether our vimentin-SunTag tracking strategy could detect perturbations to vimentin filament motion induced by known VIF modulators.

VIF motility is primarily based on MT and its motors (Gyoeva and Gelfand, 1991; Helfand et al., 2002; Hookway et al., 2015); consequently, we tracked vimentin-SunTag motility under conditions in which we experimentally manipulated the machinery responsible for MT-based transport and used our fractional motility analysis to quantify any resultant effect on global VIF motility.

First, we analyzed vimentin-SunTag tracks in either control cells or cells treated with the MT-depolymerizing agent nocodazole. We hypothesized that loss of MTs would lead to a global decrease in directed VIF transport but could potentially also reveal basal levels of MT-independent filament motion that would be otherwise undetectable. While long-term nocodazole treatment results in vimentin cytoskeletal collapse and perinuclear VIF aggregation, an outcome that would likely confound our efforts to extract MT-independent VIF trajectories, Gan et al. (2016) demonstrated that VIF spatial distribution remains largely unaffected at short intervals following MT disassembly. In line with this observation, we observed that nocodazole triggered extensive MT depolymerization within 15 min but had negligible effects on vimentin global organization at 30 min after treatment (Fig. S5).

Thus, using our vimentin-SunTag reporter, we measured the extent of VIF motility during this 15-min window following MT depolymerization in order to evaluate the extent of MT-independent VIF motion. Compared with control cells, nocodazole-treated cells showed globally reduced vimentin-SunTag motility. Single particles exhibited restricted jiggling, and we noted a threefold reduction in particles that displace >1 µm over 15 s (Fig. 4, A–D; also see Video 4).

The proper distribution of VIFs along MTs is dependent on kinesin-1 (Gyoeva and Gelfand, 1991). In RPE cells, the KIF5B isoform of kinesin-1 is the predominantly expressed isoform, and its knockout inhibits VIF transport, leading to their perinuclear accumulation, even in the presence of intact MTs (Robert et al., 2019). Here, we tested the behavior of our vimentin-SunTag reporter in RPE KIF5B-null cells. Consistent with our earlier results (Robert et al., 2019), most SunTag dots were clustered in the perinuclear region (Video 5), with a fourfold increase in stationary dots and a 3.2-fold decrease in long, linear tracks compared with the control condition (Fig. 4, A–D).

Finally, we analyzed VIF motion upon either chemical or genetic inhibition of dynein. Acute dynein inhibition with 5 µM dynapyrazole A for 45 min eliminated all long-range vimentin-SunTag trajectories, significantly increasing the fraction of spots displaying a confined motility pattern (Fig. 4, A–D and Video 6). As a complementary strategy, we overexpressed the p50 component of the dynactin complex to inhibit cytoplasmic dynein (Burkhardt et al., 1997) and observed comparable deficits in long-range transport (Fig. 4, A–D and Video 7). Compared with control cells, inhibition of dynein by either approach resulted in a decrease in long tracks by 4.8- and 3.9-fold, respectively, as well as an increase in confined, stationary spots by 3.3- and 2.7-fold, respectively. Thus, inhibition of MT-based motion, through either MT depolymerization or selective targeting of MT motors, results in the impairment of long-range VIF transport.

Notably, dynein inhibition by p50 overexpression resulted in perinuclear vimentin accumulation, reminiscent of the pattern we observed in KIF5B-null cells. The inhibition of a retrograde motor should induce a perinuclear accumulation phenotype was unexpected and strongly suggested that the activities of kinesin and dynein in VIF transport are tightly coupled.

VIF trajectories align with MTs

Given the established role of MTs in vimentin-based transport, as well as the dramatic reduction in directed motility that we detected with our vimentin-SunTag system upon inhibition of MT-based transport, we next asked whether we could use our probe to visualize individual VIF association with and translocation along MTs. As an initial control, we examined sparse vimentin-SunTag spot distribution relative to MTs in fixed, immunolabeled cells. Spots were often positioned in close spatial proximity to endogenous MTs (Fig. 5 A); however, given that vimentin-SunTag can incorporate at any position within a VIF and that VIFs are semiflexible polymers that can extend several microns in length, it is conceivable that motile SunTag spots could be positioned within a VIF at a site distal to its region of MT/motor binding. In these cases, vimentin-SunTag localizations would not necessarily overlap with MTs. Therefore, we

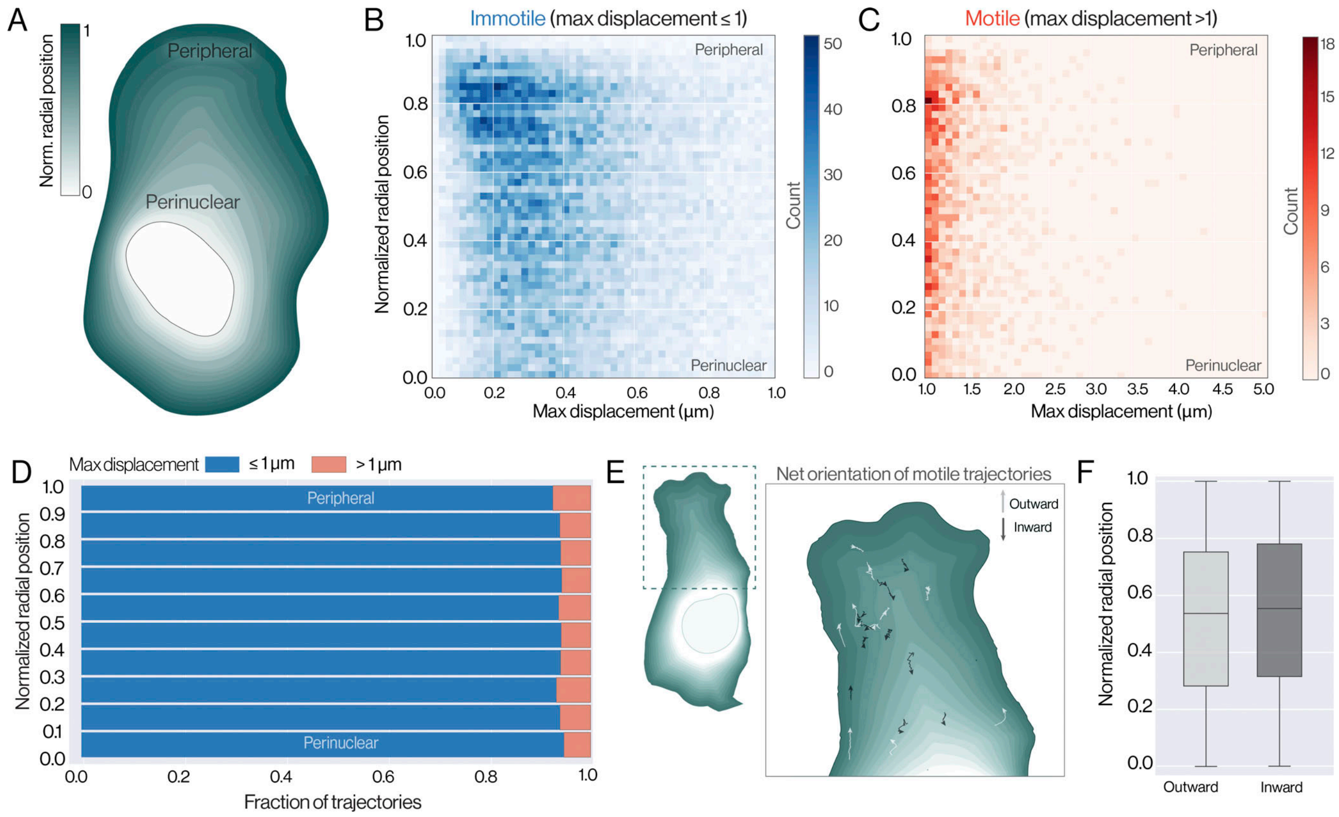

Figure 3. **VIF fractional motility is comparable in perinuclear and peripheral regions. (A)** Cartoon schematic indicating the radial normalization procedure. Irrespective of the length of the cell along any given angle, the relative position between nuclear envelope (0) and cell border (1) is computed. Perinuclear and peripheral regions are indicated. **(B and C)** Two-dimensional (2D) histograms plotting the initial normalized radial position and final maximum displacement for either immotile (B) or motile (C) 15-s trajectories. **(D)** Stacked horizontal bar plot showing the fraction of trajectories in immotile (blue) or motile (red) groups at each of the 10 normalized radial position bins. The fraction of motile trajectories is approximately equal across all radial positions. **(E)** Normalized radial position map of an RPE cell with motile (>1 µm max. disp. in 15 s) trajectories superimposed. Trajectories are classified as anterograde or retrograde by taking the difference between final and initial normalized radial positions, with positive values classified as anterograde and negative as retrograde. **(F)** Normalized radial distribution of anterograde motile VIFs and retrograde motile VIFs. Analysis was conducted on a total of 25 individual cells for each condition, collected from three independent experiments.

concluded that analyzing vimentin-SunTag trajectories relative to the path of dynamic MTs in live cells would be a more robust approach. To that end, we co-transfected vimentin-SunTag to visualize single VIFs and mCherry-EB3 to track growing MT plus ends. In cells co-expressing these markers, we observed clear alignment between motile vimentin-SunTag trajectories and the path of EB3 comets (Fig. 5 B and Video 8). Kymographs traced along EB3 paths (Fig. 5 C, i–iii) revealed a complex mix of vimentin-SunTag motility states, including stationary VIFs, as well as both anterograde and retrograde VIF transport (Fig. 5 D, iv–vi). Taken together with the inhibitor data, our correlative vimentin-SunTag kymograph analysis supports the conclusion that the majority of VIFs undergo directed transport along MT tracks.

VIFs move independently within bundles

Bundles of aligned cytoskeletal filaments are a fundamental structural feature within cells, typically formed through crosslinking individual filaments into highly ordered arrays. Among cytoplasmic IFs, keratin IFs (KIFs) are well documented to assemble into dense, tightly packed bundles, contributing to the mechanical integrity of epithelial cells (Windoffer et al., 2022; Bharathan et al., 2023). The structural organization of VIF bundles within intact cells is less clear. In vitro work using purified vimentin has shown increasing concentrations of zinc can promote the formation of loose, ionically coupled VIF bundles (Wu et al., 2020). However, a more complex reconstitution assay combining vimentin with the filament-associated protein filaggrin saw the aggregation of up to 25 VIFs into tight, microfibrillar bundles (Mack et al., 1993), suggesting a similar capacity for organized bundle formation to KIFs. Whether VIF bundles are tightly crosslinked within their native cytoplasmic environment is not clear, and existing EM micrographs of VIFs in intact cells lack the size and three-dimensional (3D) context to accurately infer bundle organization and structural properties. Consequently, in the absence of evidence to the contrary, the conventional view posits that vimentin forms dense, organized bundles in the perinuclear region that tightly confine the resident filaments. Under this model, bundled VIFs should not move independently; instead, the bundle itself acts as the functional unit of transport.

To critically evaluate this model and explicitly test whether bundled VIFs move independently or co-transport as a single

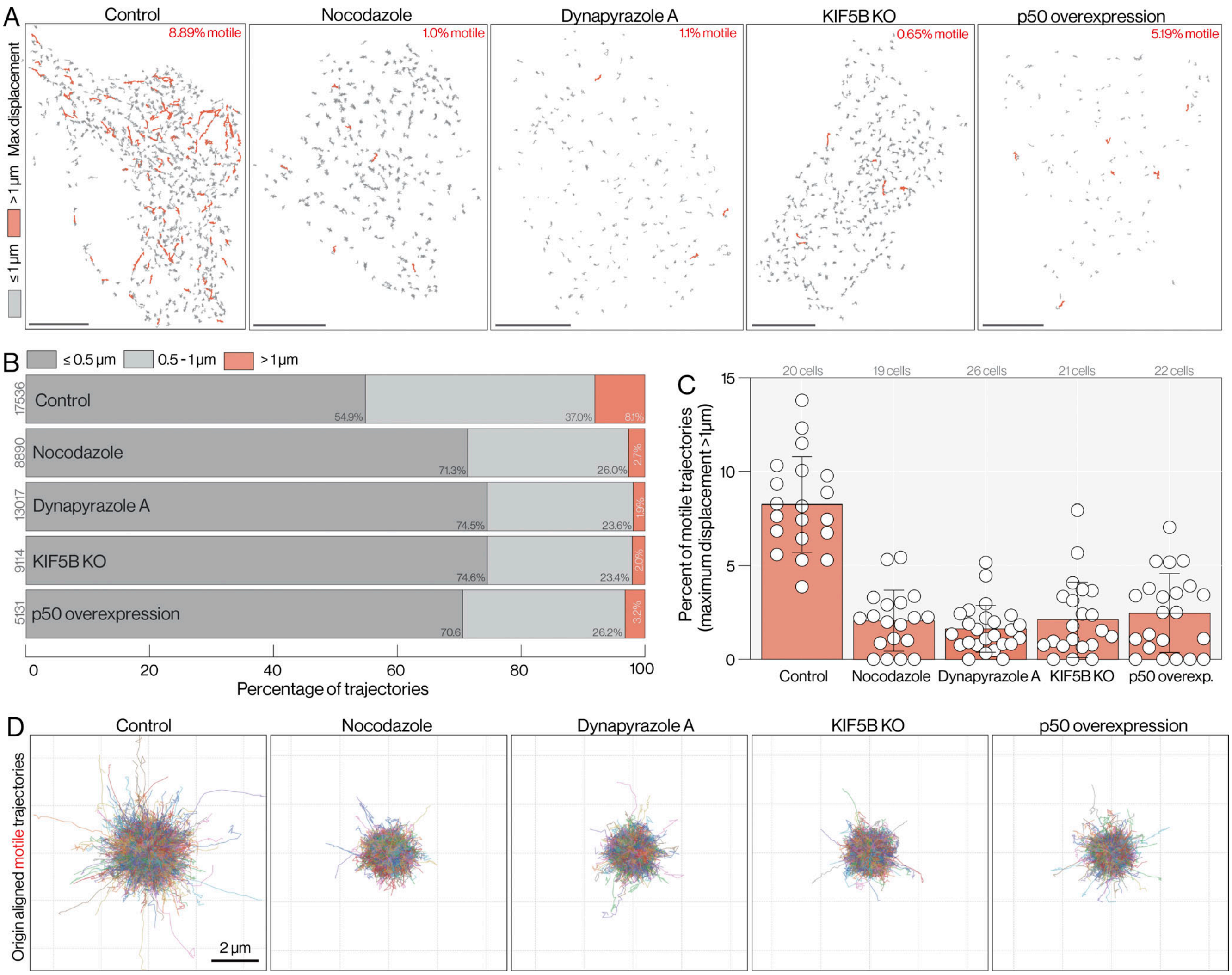

Figure 4. **Perturbation of MT-based motility abrogates directed VIF transport. (A)** 15-s vimentin-SunTag trajectories in an untreated control cell, a nocodazole-treated cell (10 µM), a KIF5B KO cell, a dynapyrazole A–treated cell (5 µM), and a p50-overexpressing cell. Motile trajectories with maximum displacements >1 µm are shown in red; all other trajectories are shown in gray. The percentage of motile tracks in each representative example is labeled in red. Scale bars = 10 µm. **(B)** Percentage of all 15-s vimentin-SunTag trajectories in each condition classified by maximum displacement into stationary (≤0.5 µm, dark gray), intermediate (0.5–1.0 µm, light gray), or motile (>1 µm, red) groups. Total tracks analyzed per condition are indicated on the left. **(C)** Percentage of motile vimentin-SunTag trajectories binned per cell for each condition. **(D)** Origin-aligned motile trajectories (>1 µm) for each condition. Trajectories are randomly colorized for visibility. Analysis was conducted on a total of 20 individual cells for each condition, collected from three independent experiments. KO, knockout.

unit, we transfected cells with an ensemble vimentin-mCherry marker to identify bundled regions, and our vimentin-SunTag tool, to identify and track single VIFs at these locations. Based on the conventional view that VIF bundles are tightly cross-linked assemblies, we hypothesized that vimentin-SunTag particles within bundles would exhibit highly correlated motion. To test this, we identified bundles in the vimentin-mCherry channel by selecting regions with high mean intensity, pronounced anisotropy, and strong orientational coherence (Fig. 6, A and B). Using kymograph analysis, we then monitored the motion of single vimentin-SunTag spots within these regions over time (Fig. 6, C and D). Contrary to our hypothesis, we observed that vimentin-SunTag spots within regions of high filament density exhibited uncorrelated motility (Fig. 6 D). Single VIFs within bundled regions often moved in opposite directions, and we frequently observed vimentin-SunTag spots spontaneously transition from stationary to directed motility, irrespective of their neighbors' behavior. These observations of dynamic and independent behavior among individual VIFs within bundles indicate that the bundles cannot be tightly cross-linked assemblies, as such cross-linking would prevent the observed independent filament movement. Therefore, our findings warrant a reevaluation of the precise structural organization of VIF bundles within intact cells.

Volume EM reveals loosely aligned, semi-coherent bundles

To directly investigate the structural organization of VIF bundles within intact cells and understand the basis for the observed independent filament movement, we employed 3D FIB-SEM. Cells were prepared as in Xu et al. (2021). In brief, cells were cultured on sapphire coverslips and cryofixed by high-pressure

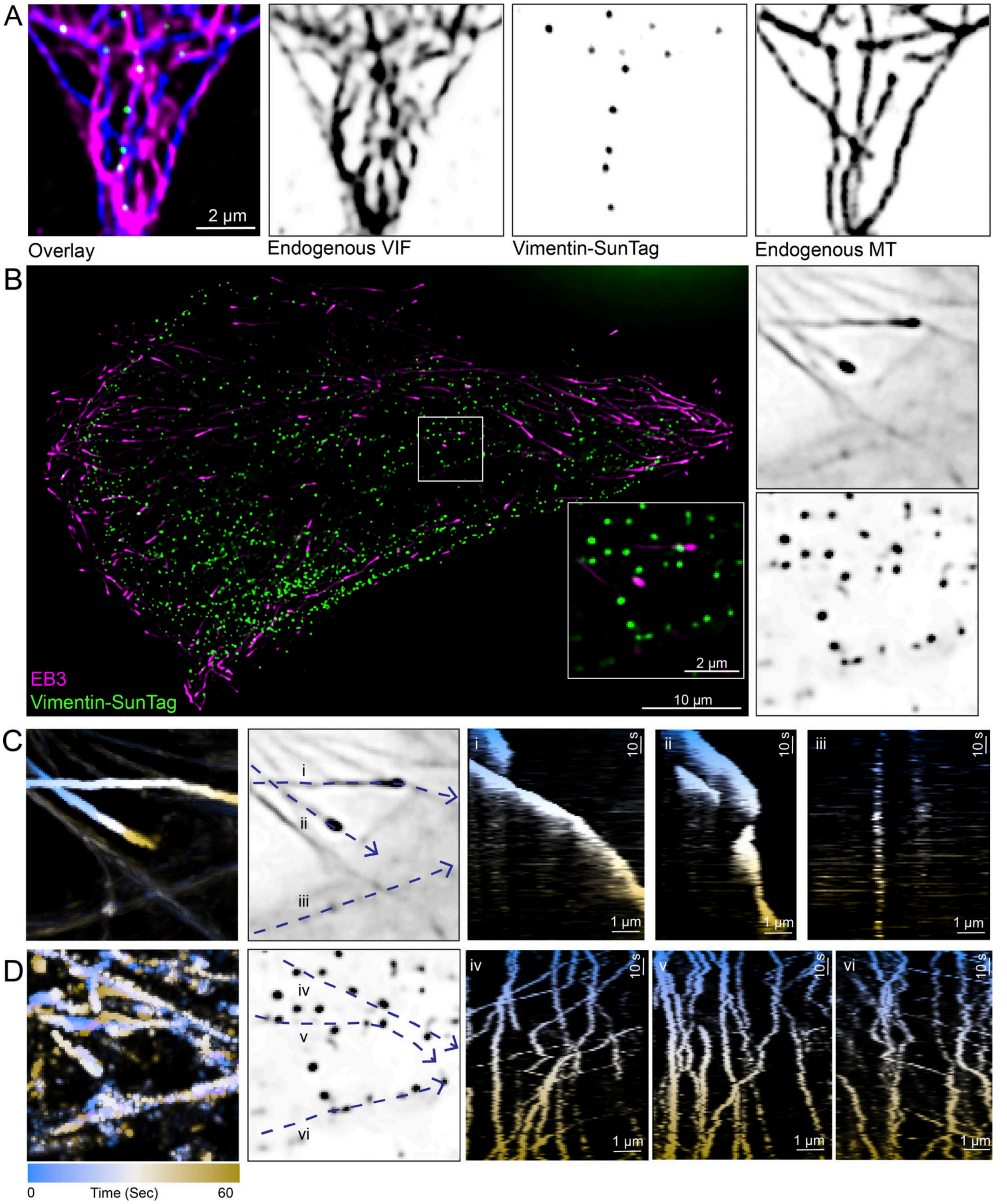

Figure 5. **Vimentin-SunTag aligns and transports along MTs. (A)** SIM micrograph of a fixed RPE cell expressing vimentin-SunTag (green) and immunolabeled for endogenous vimentin (magenta) and MTs (blue). **(B)** RPE cells co-expressing vimentin-SunTag (green) and EB3 (magenta), a snapshot from a time-lapse movie (see Video 8) captured at 2 fps over a 1-min duration. The white box highlights a zoomed-in view of the perinuclear region, showing vimentin-SunTag dots and EB3 comets. **(C and D)** Pseudocolored maximum intensity projections of EB3 comets and vimentin-SunTag particles from the zoomed-in region. The kymograph generation region for each time sequence is indicated by a blue dotted line, with arrows showing direction.

freezing (HPF). Frozen cells were then freeze-substituted in media containing osmium tetroxide and uranyl acetate before final mounting in Durcupan. FIB-SEM imaging was performed with a xy pixel size set to 2 nm and a focused Ga^+ beam set to ablate the corresponding depth of the sample surface per cycle. Raw stacks were then aligned, registered, and scaled, yielding isotropic stacks, from which a 5.0 μm × 3.0 μm × 3.6 μm subvolume in the vimentin-rich perinuclear cytoplasm was selected and processed for in-depth filament tracing and analysis (Fig. 7 A and Fig. S6 A).

Cytoplasmic IFs were identified in the FIB-SEM volume based on distinguishing features including their characteristic 12 nm cross-sectional diameter and their persistent longitudinal profiles across hundreds of consecutive slices, and by differentiating them from other similarly sized structures in the cytoplasm

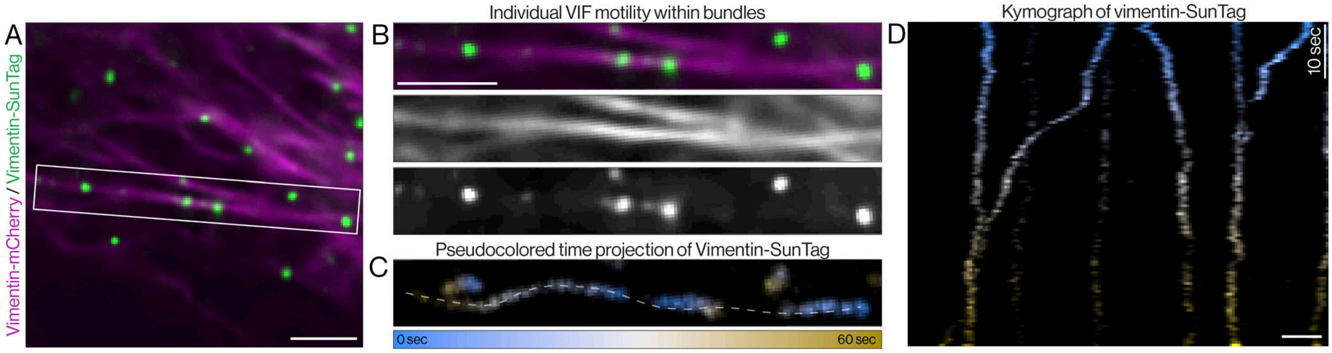

Figure 6. **VIFs move independently within bundles. (A)** Co-expression of ensemble vimentin reporter (vimentin-mCherry, magenta in overlay) and sparsely labeled vimentin-SunTag (green in overlay). **(B)** Inset from A showing a vimentin bundle sparsely labeled with vimentin-SunTag. **(C)** Pseudocolored maximum intensity time projection of vimentin-SunTag particles over 121 frames (60 s). The dashed line indicates the position of the line scan used to generate the kymograph (right). **(D)** Kymograph reveals uncorrelated movement of individual vimentin-SunTag particles within the observed vimentin bundle.

(Fig. 7, B and C). In transverse slices, filaments appeared as dark, uniform intensity spots and could be distinguished from ribosomes based on their narrower profile (11.9 versus 21.0 nm for ribosomes), decreased mean intensity, and pronounced anisotropy along their longitudinal axis (Fig. 7, C and D; Fig. S6, B and C; and Video 9). MTs were identified by their characteristic 24-nm ring-shaped cross section (Fig. S6, B and C). While our FIB-SEM staining lacks the molecular specificity to definitively confirm that these IFs consist exclusively of vimentin, immunostaining with vimentin and pan-keratin antibodies demonstrates that VIFs form the most extensive cytoplasmic filament network in COS-7 cells (Fig. S6, D–F). Furthermore, the filament bundles that we observed in COS-7 cells appeared phenotypically distinct from KIF bundles present in published, openly available FIB-SEM volumes of A431 cells (Fig. S6, G–I [Bharathan et al., 2023]), further supporting their identification as VIFs.

After completing manual annotation of the perinuclear volume, we identified and fully reconstructed nearly 600 separate VIFs representing over a millimeter of total filament lengths (Fig. 7, E–G and Video 10). Within the ∼50 µm^3 FIB-SEM volume, the reconstructed filament network displayed a pronounced radial anisotropy, with individual filaments predominantly aligned along axes radiating outward from the nuclear region toward the cell periphery (Fig. 7 E). VIFs formed an intricate, multitiered network of interconnected filament arrangements, including highly curved single VIFs, locally aligned multifilament assemblies, and thick, co-oriented filament bundles with dozens of constituent VIFs (Fig. 7, E–G). Owing to their length and flexibility, individual VIFs often spanned multiple higher order filament assemblies, resulting in a loose coupling between neighboring bundles due to their shared filaments. Bundles varied widely in width, filament count, and cross-sectional filament density (Fig. 7, H–J) and appeared notably heterogeneous, when compared not only across the network but also along their individual lengths (Fig. 7 K). Running along the longitudinal axis of a single bundle, the organization could shift dramatically—from regions of disorganized, loosely aligned filaments to segments where the filaments coalesce into ordered lateral arrays containing as many as 50 VIFs, before fraying and diverging into multiple smaller bundles (Fig. 7 E). Computational analysis of VIF distance and relative orientation to its nearest neighbors revealed a substantial fraction of co-aligned VIFs in the perinuclear region, with an average interfilament spacing of 30 nm and relative orientation of 17.8° (Fig. 7, L and M; and Video 11).

VIFs splay out from bundles to interact with MTs

Within the annotated perinuclear EM volume, we also identified and reconstructed 39 MTs representing a total length of 117 µm (Fig. 8, A–C and Video 12). Both vimentin and MT networks appeared globally co-oriented, consistent with previous light microscopy studies that have observed co-alignment between vimentin and MT networks at the macroscale (Gyoeva and Gelfand, 1991; Gan et al., 2016; Hookway et al., 2015). However, despite the common radial anisotropy shared by VIFs and MTs, we observed unexpectedly little direct local alignment between VIFs and MTs at scales and orientations that would suggest physical coupling. We had hypothesized that MTs might scaffold VIF bundles, but we observed the very opposite: VIFs within bundles appeared to be the least likely filaments to interact with MTs.

To quantitatively assess the spatial relationship between VIFs and MTs, we calculated the average distance and relative orientation angle between each VIF and its closest MT neighbor. In contrast to the tight 30-nm average distance and 17.8° relative orientation between neighboring VIFs, we calculated a mean VIF to MT neighbor distance of 233 nm and mean relative orientation of 33.2°. Plotting these distributions for all filaments in the volume revealed that only a small fraction of vimentin filaments were both closely positioned (within 100 nm) and co-oriented (within 20°) with MTs (Fig. 8 D). Using these thresholds, ∼11% of VIFs were closely aligned with MTs, a proportion notably similar to the constant fraction of VIFs undergoing directed transport in our live-cell imaging experiments (∼8%).

Recognizing that averaging local nearest MT neighbor distances and relative orientations across full VIFs might obscure brief but physiologically relevant coupling events that would represent only a small proportion of total VIF length, we performed a higher resolution analysis by sampling points every 4 nm along each VIF and calculating the NND and relative orientation to the nearest MT at each point. To visualize this relationship, we then color-coded the nearly 600 reconstructed vimentin filaments in our dataset

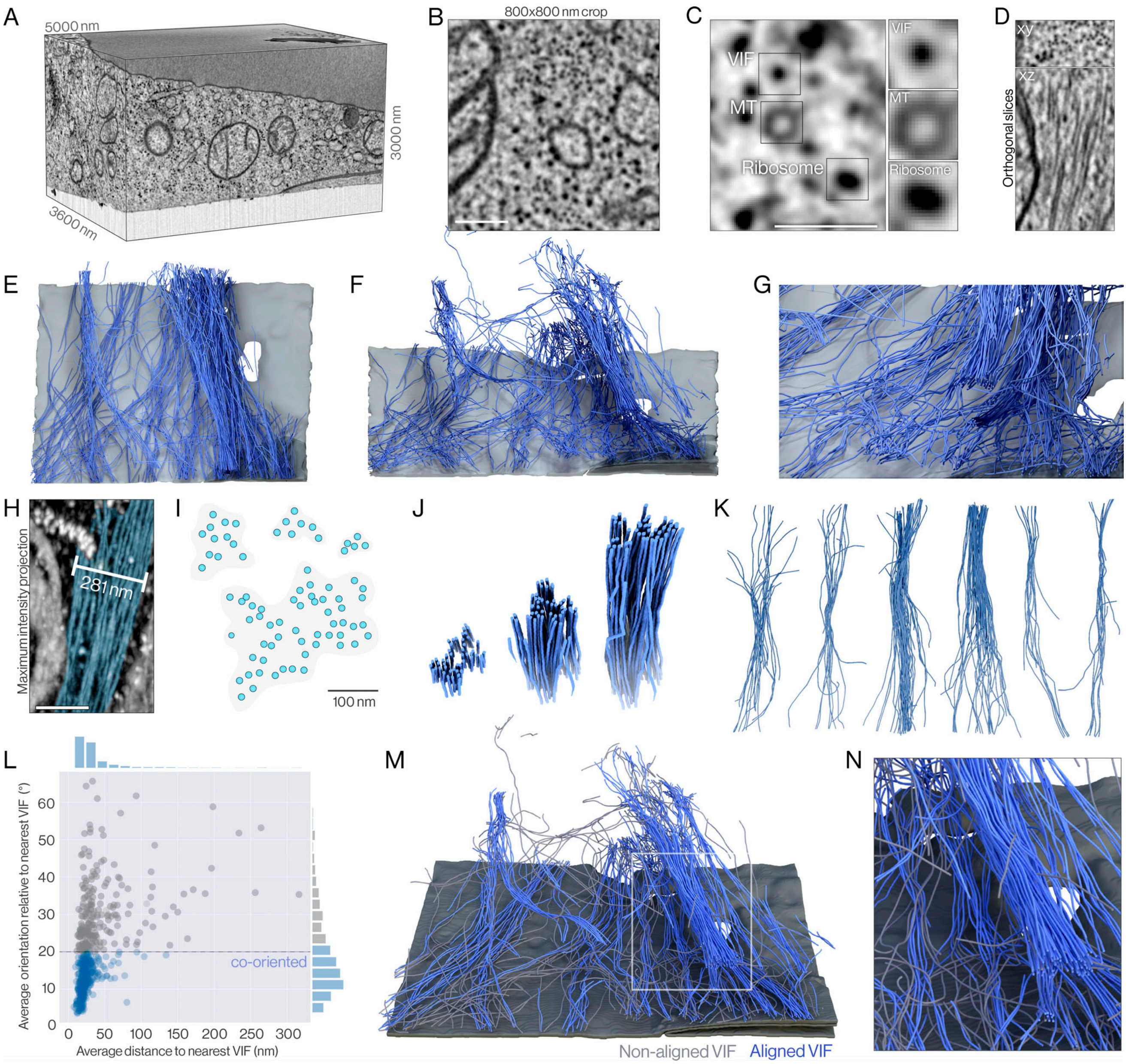

Figure 7. **Perinuclear VIFs are loosely aligned within disorganized bundles.** **(A)** 3D bounding box corresponding to the analyzed perinuclear FIB-SEM volume. **(B)** Representative slice cropped from this volume depicting staining density within the crowded cytoplasm. Scale bar = 200 nm. **(C)** Cropped FIB-SEM slice with magnified insets indicating cross-sectional profiles of a VIF (top), an MT (center), and a ribosome (bottom); different z slices from this stack are represented in Fig. 8 G. **(D)** Orthogonal FIB-SEM slices centered on a VIF bundle indicating representative transverse and longitudinal VIF profiles. **(E–G)** 3D reconstructions of VIFs (blue) traced from the FIB-SEM volume. The ventral plasma membrane is indicated in gray. **(H)** Maximum intensity projection of a FIB-SEM subvolume featuring a thick vimentin bundle (blue overlay). Scale = 200 nm. **(I)** Segmented filaments (blue dots) in a cross section through a VIF bundle. The four shaded areas indicate subregions of filament clustering within the larger bundle architecture. **(J)** 3D rendering of a VIF bundle clipped at three positions to reveal differences in relative filament positioning. **(K)** Aligned montage of isolated VIF bundles derived from the volume indicated in A. **(L)** Scatter plot indicating average orientation relative to first nearest neighbors and average distance to first nearest neighbors for traced filaments. The dashed line indicates 20° threshold for co-orientation. **(M)** Rendering of perinuclear VIFs color-coded by orientation relative to nearest neighboring filaments. Blue indicates aligned filaments (relative orientation <20°), while gray indicates nonaligned filaments (relative orientation >20°). **(N)** Magnified inset indicating blue aligned filaments within a bundle and neighboring gray, nonaligned, curved VIFs.

based on local alignment. Specifically, we used a 5-node sliding window average to first smooth distance/orientation measurements, then color-coded any 4-nm VIF segment that was locally co-oriented with an MT within a relevant interaction distance (20° relative orientation, 100-nm neighbor distance, Fig. 8 E). This point-wise mapping confirmed that VIFs do not co-align with MTs along their entire longitudinal axis, but did reveal numerous short segments of transient VIF-MT pairing, as well as local hotspots with enhanced rates of vimentin–MT alignment, which often occur at sites of VIF bundle fraying (Fig. 8, C and E). Overall, ~9.8% of

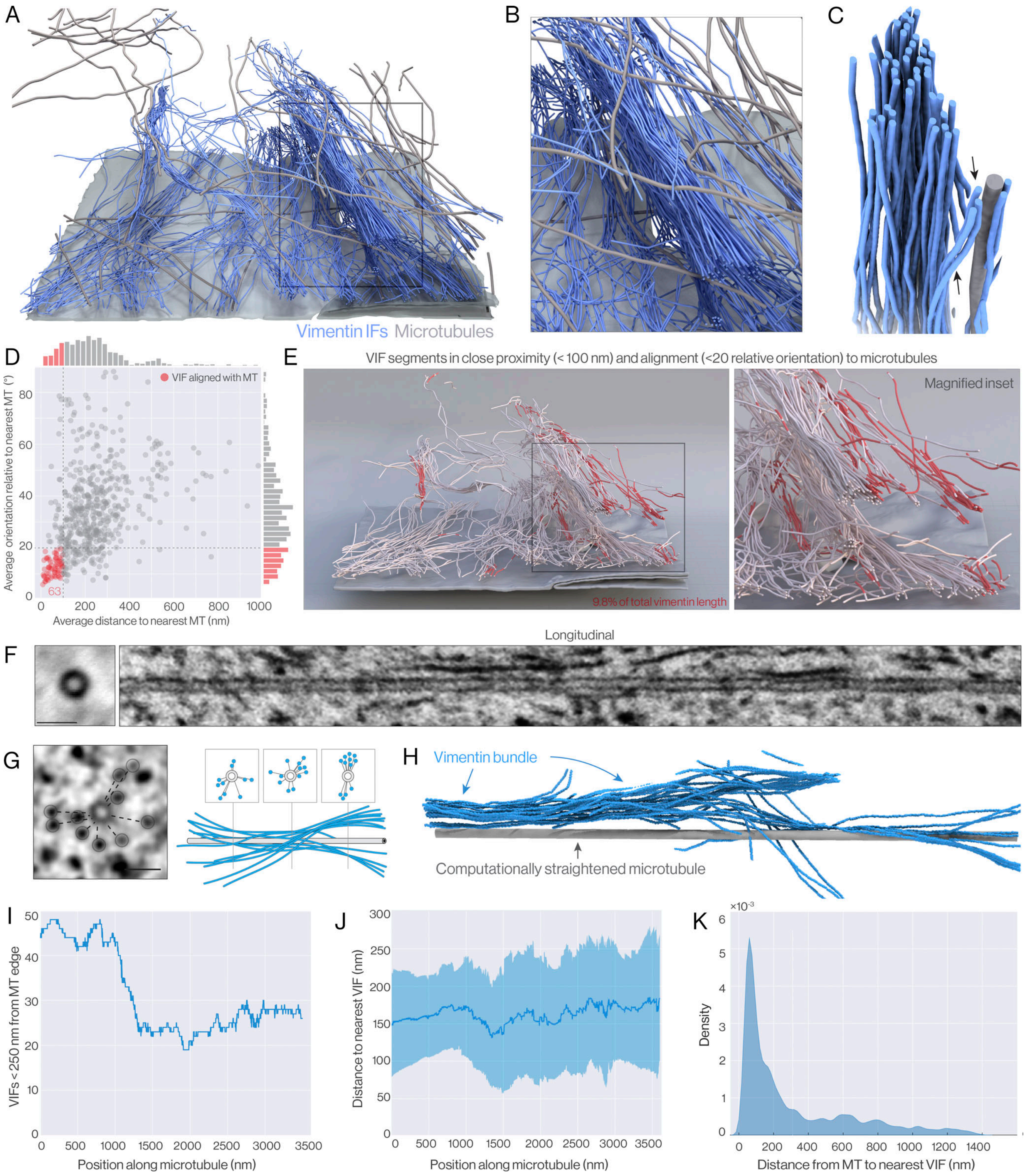

Figure 8. **VIFs defasciculate from bundles to interact with MTs. (A)** 3D rendering of VIFs (blue) and MTs (gray) traced from the EM volume specified in Fig. 7 A. The ventral plasma membrane is shown in light gray. **(B)** Magnified inset of a VIF bundle and neighboring, minimally co-aligned MTs. **(C)** 3D reconstruction of a VIF bundle (blue) aligned with an MT (gray). VIFs at the bundle surface splay out, locally aligning with the MT (black arrowheads). **(D)** Scatter plot with marginal histograms indicating average VIF orientation relative to the nearest MT versus average VIF distance to the nearest MT. **(E)** Rendering of perinuclear VIFs color-coded by local alignment with MTs. VIF segments that are both proximity to and aligned with a neighboring MT (<100 nm NND and <20° relative orientation) are red. All other nonaligned segments are white. **(F)** Sum intensity projection of a center-aligned 3,500-nm MT trajectory. Scale bar = 50 nm. (Right) Orthogonal view of an MT center–aligned track. By aligning the stack around the MT centroid, we have computationally straightened the MT, allowing for visualization of the local neighborhood around a single MT. **(G)** MT-centered FIB-SEM slice with VIF cross sections highlighted by blue circles and distances from the MT delineated by the dashed lines. Scale bar = 50 nm; different z slices from this stack are represented in Fig. 7 C. (Right) Cartoon schematic

relating the cross-sectional profile of MTs and vimentin to the expected appearance in the longitudinal axis. **(H)** 3D reconstruction of a computationally straightened MT (gray) and local vimentin filament bundle (blue). **(I)** Total number of vimentin filaments within 249 nm of the centroid of an MT over its 3,500-nm length. **(J)** Average distance of vimentin filaments from a single MT over its 3,500-nm length within the reconstruction volume. Line = mean, error bars = standard deviation. **(K)** Distribution of distance between MTs and their nearest vimentin neighbors. The line indicates a mean distance of 309 nm.

the total fraction of perinuclear VIF length was aligned with MTs, again comparable to the fraction of VIFs exhibiting directed transport.

As a complementary approach, we examined the spatial relationship from the perspective of MTs. Using a computational straightening technique, we generated MT-centered subvolumes (Fig. 8 F), allowing us to visualize the organization and proximity of VIFs relative to the MT edge (Fig. 8, G–J). Nearest neighbor analysis of ~30,000 MT vertices revealed an average distance of 309 nm to the closest vimentin surface (Fig. 8 K). Indeed, over 85% of all MT voxels were positioned at >50 nm from the nearest VIF and we did not observe any examples in which an MT appeared to scaffold or support the core of a vimentin bundle.

While the limited nanoscale spatial proximity between VIFs and MTs might seem inconsistent with the clear macroscale co-alignment observed in previous studies, our data indicate that direct and sustained physical interactions are not necessarily required for cytoskeletal crosstalk. Even infrequent interactions at discrete sites may be sufficient to coordinate global alignment between the VIF and MT networks. Additionally, indirect interactions mediated by extended linker proteins or molecular motors could facilitate coupling without requiring close proximity between the filaments.

VIFs in the distal cell periphery display reduced co-orientation and increased proximity to MTs

As a comparison with the dense vimentin network in the perinuclear region, we elected to reconstruct VIFs and MTs in the flat peripheral region of the vimentin cytoskeleton (Fig. 9). To accomplish this, we acquired an additional FIB-SEM stack of a separate COS-7 cell imaged at a 4-nm isotropic resolution. We selected a 9.10 × 3.35 × 0.57 µm subvolume in the flat cell periphery and repeated the same procedure for VIF identification, tracing, and analysis as we had used for the perinuclear dataset. We observed a far more equal ratio of VIF to MT length (153-µm VIF and 102-µm MTs), compared with the nearly 10:1 ratio of vimentin to MTs in the dense perinuclear region. Given the constrained cellular geometry in the much flatter cell periphery, VIFs and MTs were all aligned within the same lateral plane (Fig. 9, A–C).

In comparison with the perinuclear volume, we did not observe extensive VIF bundling in the peripheral region (Video 13). In fact, across the entire peripheral volume, we observed decreased co-orientation between neighboring vimentin filaments (Fig. 9 D). Furthermore, we observed that peripheral VIFs appeared to more closely align with MTs, as indicated by a reduced distance between VIFs and their nearest MT neighbors (Fig. 9 D), as well as a larger fraction of VIF length satisfying our distance and orientation threshold for local alignment (24.6% of total peripheral VIFs compared with 9.8% of perinuclear VIFs). Of note, despite this higher fraction of peripheral VIFs co-aligned with MTs, the total length of VIFs aligned with MTs in the periphery (37.6 µm) was still substantially less than that in the perinuclear region (106 µm), due to the significantly lower abundance of VIFs in the peripheral region.

The differences that we observe in VIF organization between perinuclear and peripheral regions support a model in which the extent of VIF-MT interaction is inversely correlated with the propensity of VIFs to bundle. In regions where VIFs are densely bundled and outnumber MTs by ~10:1, direct interactions with MTs are limited, possibly due to steric hindrance or a higher likelihood of VIF-VIF lateral associations. Conversely, in peripheral regions with a lower density of VIFs and a closer ratio of VIFs to MTs (~1:1), individual filaments are more likely to interact directly with MTs.

Discussion

In this study, we employed the multimeric fluorescent SunTag labeling approach to sparsely tag and identify single vimentin filaments in live cells. We confirmed vimentin-SunTag integration into single VIFs using structured illumination microscopy (SIM) imaging and PREM and validated that its expression did not disrupt the organization of the endogenous VIF cytoskeleton. Using this reporter, we tracked single VIFs in all regions of the cytoplasm, including in the previously inaccessible, densely packed perinuclear vimentin network. Surprisingly, even in these extraordinarily dense regions, vimentin-SunTag showed extensive motility, a level of VIF dynamics not previously observed with other imaging techniques. While subtle effects of labeling cannot be entirely ruled out, our PREM and SPT analyses indicate that SunTag labeling does not alter the structure or motion of endogenous VIFs. Vimentin-SunTag imaging enables the monitoring of both global and localized VIF dynamics in real time, facilitating the precise study of VIF dynamics in various cellular contexts, both globally and at specific regions of interest.

We consistently noted multiple vimentin-SunTag spots within the same bundle exhibiting independent movement, occasionally even in opposite directions. Concurrently, some particles within the same bundle either remained stationary or underwent short displacements. These observations represent the first evidence that the motility of vimentin filaments within a given bundle is often uncoordinated and suggest that the lateral attractive forces holding the bundled filaments together can be readily overcome by motor-based pulling. Supporting this weak VIF bundling model, 3D reconstructions of VIF bundles revealed loose-packed arrays with the fluctuating filament number and packing density. VIF bundles appeared frayed, unraveling along their length as single VIFs intermittently peeled away from the bundle periphery to transiently realign with neighboring MTs. Of note, these vimentin–MT junctures were brief and infrequent compared

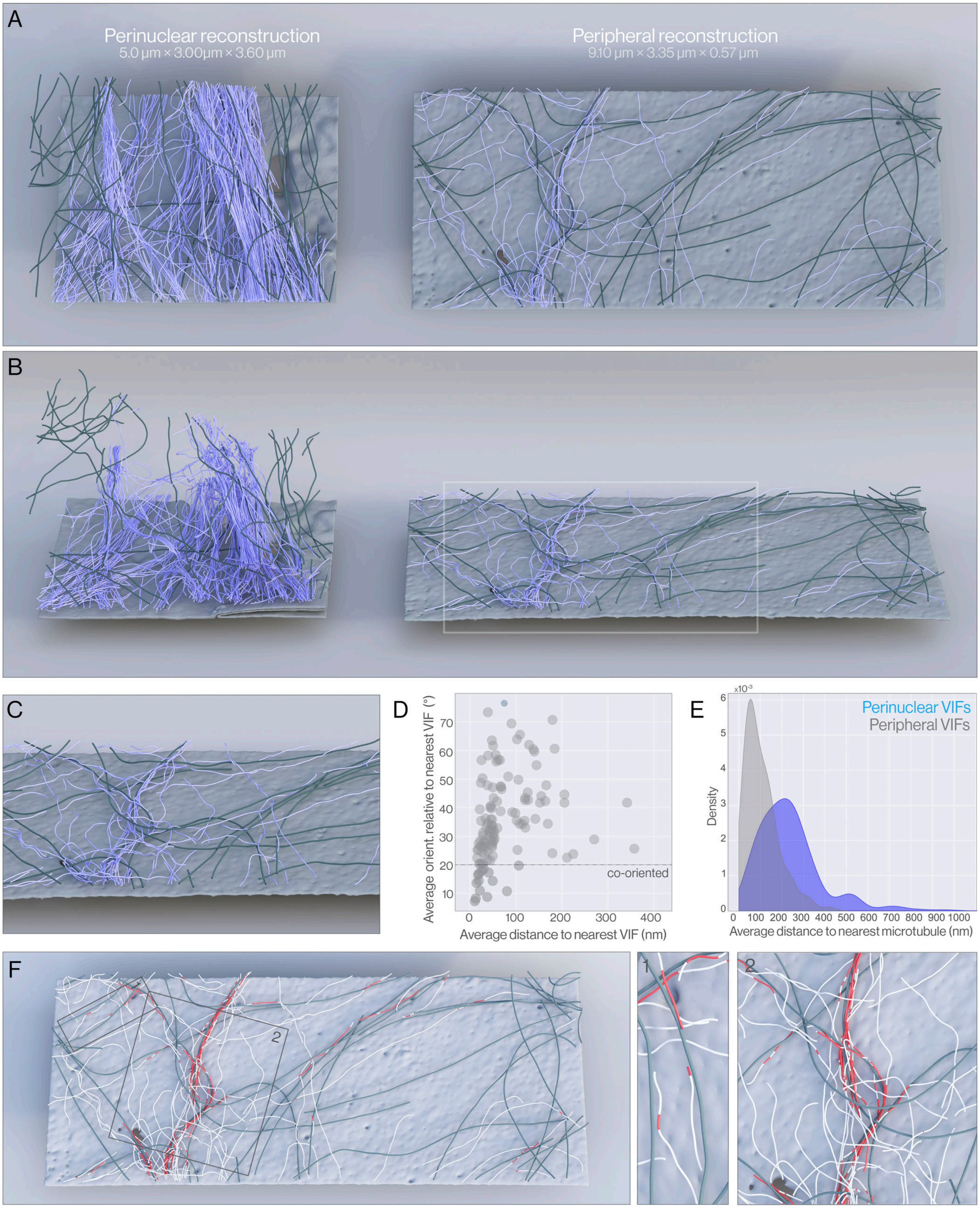

Figure 9. **VIFs display reduced filament alignment and increased MT association in the sparse peripheral vimentin cytoskeleton. (A and B)** Top-down (A) and oblique (B) 3D renderings of VIFs (blue), MTs (dark gray), and plasma membrane (light gray) reconstructed from perinuclear (left) and peripheral (right) subvolumes. **(C)** Magnified inset of perinuclear reconstruction indicated by the white box in B. **(D)** Scatter plot indicating average peripheral VIF-to-VIF neighbor distances and relative orientations. The dashed line indicates 20° co-orientation threshold. **(E)** Distribution of average NND between VIFs and MTs in

either perinuclear (blue) or peripheral (gray) VIF networks. **(F)** Rendering of peripheral VIFs color-coded by local alignment with MTs. VIF segments that are both in proximity to and aligned with a neighboring MT (<100 nm NND and <20° relative orientation) are coded red. All other nonaligned segments are coded white. MTs are shown in dark gray, and the plasma membrane beneath is indicated in light gray. Inset 1 indicates peripheral VIFs that locally couple to the MT over short segments. Inset 2 indicates a hotspot with extensive VIF-MT co-alignment.

with the total length of each filament. In general, we observed a marked separation between bundled VIFs and MTs with surprisingly low levels of direct interaction. The sporadic nature of this physical vimentin–MT coupling may account for how motors and their cargoes can successfully traverse seemingly impenetrably dense regions of the vimentin filament cytoskeleton. In light microscopy movies, the subtle offset between VIF bundles and underlying MTs is not as clearly apparent as in our 3D reconstructions from FIB-SEM volumes. Were the VIF bundles to instead enmesh MT tracks, this tight coupling could potentially occlude molecular motor binding and stall organelle trafficking leading to defects in subcellular organization. Together, our novel approaches to visualize vimentin reveal that VIF bundles are not tightly cross-linked structures akin to dense actin bundles, but rather weakly associated filament arrays from which single VIFs can freely enter and exit. This study offers a fresh perspective on VIF organization and dynamics within the cellular milieu. Future investigations could explore how VIFs are organized and behave during various cellular events and across different cell types, deepening our understanding of their roles in cellular processes.

FIB-SEM acquisition and subsequent VIF tracing are inherently of low throughput; consequently, we examined only subvolumes from two different cells. However, there is a large and constantly growing body of publicly available FIB-SEM data that can be used for IF tracing. Developing automated methodologies for identifying and reconstructing IFs from these datasets will undoubtedly yield new insights into IF structure and organization. Based on our 3D reconstruction and vimentin-SunTag tracking, we can envision several mechanisms by which VIFs could either dampen or stimulate intracellular trafficking in response to cellular needs. On the one hand, a dense intracellular vimentin mesh may act as a brake or anchor on MT-based organelle motion. In this scenario, VIFs may interact with passing organelles, either directly via a molecular linker or indirectly through nonspecific obstruction, slowing or stalling organelle motion via an increased drag or occlusion of motor binding sites. Alternatively, given the binding affinity of vimentin for both motor proteins (Gyoeva and Gelfand, 1991; Robert et al., 2019; Prahlad et al., 1998; Helfand et al., 2002) and membranous organelles (Vitali et al., 2023; Nekrasova et al., 2011; Biskou et al., 2019; Schwarz and Leube, 2016), it is not implausible that VIFs could also behave as motor adaptors. Cytoskeletal filaments, including MTs, IFs, and microfilaments, are intertwined within the cytosol and interact through cytolinkers or signaling events (Chang and Goldman, 2004; Seetharaman and Etienne-Manneville, 2020; Pradeau-Phélut and Etienne-Manneville, 2024). These interactions play a crucial role in both the organization and the transport of IFs. Cytolinkers such as plectin (Burgstaller et al., 2010), fimbrin (Correia et al., 1999), and filamin-A (Kim et al., 2010) mediate interactions between IFs and actin, influencing the role of IFs in focal adhesion and filopodium formation in migrating cells. Phosphorylated mitogen-activated protein kinases Erk1 and Erk2 have been implicated in the retrograde transport of VIFs (Perlson et al., 2005). However, the molecular mechanism behind these interactions requires further investigation.

By providing multiple binding sites along its length, a vimentin filament could engage motor proteins and thereby stimulate robust directed transport of a given cargo. Further, the regular, repeating geometry of a vimentin filament may also serve to array multiple cargoes or scaffold motor teams onto structures that would otherwise lack sufficient surface area to accommodate such bulk. Lastly, VIFs may even accommodate motor-based sliding of single or multiple MTs and therefore play important roles in cytoskeletal patterning. This concept that vimentin may act not simply as passive cargo but as a dynamic versatile motor adaptor opens exciting new possibilities toward understanding the complex regulatory mechanisms underlying intracellular trafficking.

Cellular transport is the coordinated function of both MT and actin-based systems (Langford, 1995; Rogers and Gelfand, 1998). The long, linear transport of vimentin-SunTag–labeled single filaments is lost after depolymerization of MTs. Additionally, the disruption of MT motor function through either genetic modification or chemical inhibition leads to a significant decrease in long-range anterograde and retrograde transport. These observations suggest that transport of VIFs by the plus-end MT motor kinesin-1 and the minus-end motor cytoplasmic dynein is coordinated, a property that we observed in the past for the transport of membrane organelles (Kural et al., 2005; Hendricks et al., 2010; Barlan et al., 2013).

Previous studies have extensively documented interactions between VIFs and actin filaments (Hollenbeck et al., 1989; Wu et al., 2022; Esue et al., 2006). The possibility arises that the short-range movement of VIFs may depend on the actin cytoskeleton and its associated motor proteins. Vimentin-SunTag can serve as an excellent tool to address and investigate this intriguing question, providing a platform to explore the interplay between VIFs and the actin cytoskeleton in cellular dynamics. We hypothesize that the occurrence of short pauses and directional reversals in VIF–cargo transport along MT tracks may be the result of a molecular tug-of-war or a coordinated action between MT motors (kinesin-1 and dynein) and actin motors (myosin) (Evans et al., 2014; D'Souza et al., 2022, *Preprint*; Vale, 2003). The mechanisms underlying this molecular tug-of-war are not fully understood; however, we believe that specific adaptors or linker proteins bind to cargoes.

Materials and methods

Plasmids

The SunTag system plasmids pcDNA4TO-K560-E236A-24xGCN4_v1-IRES-Puro (plasmid #60909; Addgene; RRID: Addgene_60909) and pHR-scFv-GCN4-sfGFP-GB1-NLS-dWPRE (sfGFP) (plasmid #60906; Addgene; RRID: Addgene_60906) were generously provided by

Ron Vale (Tanenbaum et al., 2014). The K560-E236A sequence in pcDNA4TO was replaced with vimentin cDNA tagged with a 3X Flag-tag, resulting in the fusion of a 24xGCN4 peptide epitope array to the C terminus of a vimentin-3X Flag sequence. To achieve sparse labeling with the vimentin-24xGCN4 fusion, the construct was subcloned into a pLVX-CMV100 lentiviral backbone (gift from Kevin Dean & Reto Fiolka [plasmid # 110718; Addgene; RRID: Addgene_110718]), which carries a truncated CMV promoter comprising only the first 100 base pairs (CMV100). Genes expressed under CMV100 display reduced expression levels as compared to those expressed under longer CMV truncations or the full-length CMV promoter (Dean et al., 2016; Mohan et al., 2019). Human dynamitin (p50) cDNA was inserted into the pEGFP-1 plasmid backbone between the EcoRI and BamHI sites, and the EGFP cDNA was replaced with mCherry cDNA. The vimentin-mCherry plasmid was generated by replacing the p50 with vimentin cDNA in the same plasmid between the EcoRI and BamHI sites.

Cell cultures

Human RPE cells (ATCC) were cultured in DMEM (#D5648; Sigma-Aldrich) supplemented with 10% fetal bovine serum and maintained at 37°C with 5% CO_2. The kinesin-1 (KIF5B) knockout RPE cell line was previously generated in our laboratory (Robert et al., 2019). For imaging experiments, cells were seeded onto clean 22-mm square glass coverslips (AmScope, 0.12–0.16 mm thickness) in 35-mm dishes. For SIM imaging, cells were seeded onto 18-mm square glass coverslips (No. 1.5 cover glass; Corning). Plasmid transfections were performed the following day using Lipofectamine 3000 Transfection Reagent (#3000-008; Thermo Fisher Scientific) or ViaFect (#E498A; Promega) following the manufacturer's protocols. To achieve sparse labeling, we optimized DNA concentrations for transfection, using 1 µg of pHR-scFv-GCN4-sfGFP-GB1-NLS-dWPRE and 0.5 µg of pLVX-CMV100-Vim-24XGCN4 plasmids per 35-mm dish, maintaining a precise 2:1 ratio. Imaging was performed 24 h after transfection. To induce MT depolymerization, cells were treated with 10 µM nocodazole. Cytoplasmic dynein was inhibited using 5 µM dynapyrazole A (#6896; Tocris).

Spinning disk confocal microscopy

Live-cell time-lapse sequences were captured using a Nikon Eclipse Ti2 stand equipped with a W1 spinning disk confocal head (Yokogawa CSU with a pinhole size of 50 µm), utilizing either a 60× 1.49 N.A. or a 100× 1.45 N.A. oil-immersion lens. Image acquisition was performed with a Hamamatsu ORCA-Fusion Digital CMOS camera (Model: C13440-20CU) driven by Nikon NIS-Elements software (version 5.42.01). iChrome MLE Laser (serial #30380; Topica) served as the light source. A Tokai Hit stage-top incubator and an Okolab gas mixer were employed to maintain a constant temperature of 37°C and a CO_2 level of 5%.

Structured illumination microscopy

Images were acquired using CrestOptics DeepSIM X-Light (#S8002) mounted on the Nikon Eclipse Ti microscope stand, equipped with a Plan Apo λ 60× /1.4 N.A. oil-immersion objective lens. The Celesta light engine (#80-10268; Lumencor) served as the light source. The light emitted from the samples passed through specific band-pass filters (Chroma, blue channel: #ET440/40m; green channel: #ET510/40m; red channel: #ET590/50m; far-red channel: #ET690/70m) corresponding to their respective fluorescent channels. Images were captured by a Teledyne photometric BSI sCMOS camera controlled by Nikon NIS-Elements software (version 5.42.03). In the DeepSIM module (65 images per focal plane), Z-stack images were acquired at intervals of 0.1 µm/step. The raw images were reconstructed into SIM images using the SIM reconstruction module in Nikon NIS-Elements software.

Immunofluorescence of RPE cells

24 h after transfection, RPE cells were prefixed for 3 min at 37°C in a solution of 0.3% glutaraldehyde and 0.2% Triton X-100 in PHEM buffer (60 mM Pipes, 27 mM Hepes, 10 mM EGTA, 8 mM $MgSO_4 \cdot 7H_2O$, pH 7.0). Cells were then postfixed for 15 min at 37°C with 4% paraformaldehyde in PHEM buffer. After fixation, cells were quenched in 5 mg/ml sodium borohydride for 5 min to neutralize free aldehyde groups, followed by three 5-min washes in 1x PBS. Next, cells were incubated with a blocking solution of 2.5% BSA for 45 min at room temperature. Cells were then incubated with primary antibodies against MTs (DM1α, mouse monoclonal, in-house, 1:1,000) and vimentin (chicken, #919101; BioLegend, 1:2,000) for 45 min at room temperature in blocking solution. Following primary antibody incubation, cells were washed and incubated with secondary antibodies: rhodamine-conjugated goat anti-mouse IgG and Alexa Fluor 647–conjugated donkey anti-chicken IgG (#115-025-003 and #703-605-155; Jackson ImmunoResearch, 1:700) for 45 min in blocking solution. After both primary and secondary antibody incubations, cells were washed with 0.2% Tween-20 in PBS, followed by a final rinse in PBS. Coverslips were then mounted with Mowiol and allowed to cure for 24 h at room temperature before DeepSIM imaging.

Immunofluorescence of COS-7 cells

COS-7 cells plated on #1.5 glass-bottom dishes (MatTek) were grown to 70% confluency and fixed in −20°C methanol for 5 min followed by three times of washes in PBS. Cells were then incubated in 1xPBS with 2% BSA containing primary antibodies against vimentin (chicken, CPCA-Vim; Encor, 1:1,000) and alpha-tubulin (mouse, T6199; Sigma-Aldrich, 1:1,000) overnight at 4°C. The next day, cells were washed three times in PBS and incubated with goat anti-mouse Alexa Fluor 488 Plus (A28175; Invitrogen, 1:1,000) and goat anti-chicken Alexa Fluor 555 Plus (A32932; Invitrogen, 1:1,000) for 45 min in PBS before a final three times of wash in PBS. Samples were imaged in PBS.

Immunogold staining and EM of platinum replica

Cells labeled with vimentin-SunTag were extracted and fixed using a previously described protocol (Renganathan et al., 2023). RPE cells were seeded and transfected onto glass coverslips as described above. In order to extract membrane and soluble cytosolic proteins, cells were incubated in 1% Triton X-100 in PEM buffer (80 mM Pipes, 1 mM EGTA, 1 mM $MgCl_2$ at pH 6.8) for 5 min. Cells were next treated with 0.6 M potassium chloride in PEM buffer for 10 min in order to remove MT and actin filaments from the residual cytoskeletons still attached to the coverslips. Samples were then fixed with 2% glutaraldehyde in 0.1 M cacodylate buffer. Subsequently, the cells were incubated with a rabbit anti-GFP antibody (#6556; Abcam) and then probed with a secondary antibody goat anti-rabbit tagged with 12-nm colloidal gold (#111-205-144; Jackson ImmunoResearch). PREM was performed as previously described (Svitkina, 2009; Korobova and Svitkina, 2008). Samples were imaged using a FEI Tecnai Spirit G2 transmission electron microscope (FEI Company) operated at 80 kV. Images were captured by an Eagle 4k HR 200 kV CCD camera. Gold particles were manually pseudocolored in Adobe Illustrator.

Vimentin-SunTag image preprocessing and analysis

Image processing was performed using ImageJ 1.54f (Schindelin et al., 2012) and loaded with the Bio-Formats Importer plugin (Linkert et al., 2010). To correct photobleaching, a bleach correction was applied to each image using the histogram matching method (Miura, 2020). Background correction was performed by subtraction of the minimum intensity projection. Color-coded maximum intensity time projections were generated using the temporal color code function.

Vimentin single-particle localization and SPT

Images were processed in ThunderSTORM (Ovesný et al., 2014) using a wavelet filter (B-spline, scale 2.0, order 3). SunTag spots were identified using local maximum detection with an eight-neighborhood setting and thresholding at 1 standard deviation. The Gaussian fitting yielded subpixel localization coordinates, as well as measurements for sigma (spot width) and uncertainty (localization precision), reflecting the spot size and localization accuracy, respectively. Spot intensity was recorded to infer the extent of scFv-GCN4-sfGFP binding at each vimentin-SunTag spot. Localized particles were linked across frames using the LAP tracker (Jaqaman et al., 2008). Tracks were linked using a maximum linking distance of five pixels and a gap closing maximum frame gap of two frames. Frame gaps were closed through linear interpolation.

Track standardization

To ensure consistent track durations and facilitate meaningful comparisons between trajectories, all tracks were standardized to 30 frames (15 frames). Specifically, trajectories shorter than 30 frames were excluded, while those longer than 30 frames were segmented into as many nonoverlapping 30-frame sections as possible, with any remaining frames discarded. This approach ensured that all retained segments had the same duration, allowing for a fair comparison across trajectories in subsequent displacement analyses.

Following this standardization, we calculated edge features including instantaneous speed, displacement, and angle change. From these, we then computed track features, including mean and maximum speed, net displacement (distance from the first to the last step of the track), maximum displacement (maximum distance from the first step to any point in the track), total distance (sum of all frame-to-frame displacements), directionality ratio (ratio of net displacement to total distance), and mean directional change (average angle change between all steps in a track). Trajectories were binned based on maximum displacement class using a threshold of >1 μm displacement over 30 frames to indicate motile trajectories, and a threshold of either ≤1 μm or ≤0.5 μm to indicate immotile or stationary trajectories.

Standardized trajectories were also used to compute MSD velocity autocorrelation over 15 lags. Sliding window MSD and alpha fitting: We performed a sliding window MSD analysis by dividing each trajectory into overlapping 20-frame subtrajectories. For each subtrajectory, MSD was computed and subsequently fit to a power law model, $MSD(\tau) = 4D\tau\alpha$, to extract local alpha values, allowing us to categorize motility behavior across different trajectory segments.

To enable precise spatial analysis, distinct cellular regions were mapped to represent nuclear, perinuclear, and cytoplasmic areas. Nuclear and periphery boundaries were initially traced manually in ImageJ, ensuring that both boundaries had an equal number of points. These tracings provided the foundation for generating binary masks that defined each region, allowing consistent and accurate classification of particle locations within nuclear, perinuclear, and cytoplasmic compartments.

Spatial analyses

Spatial analyses were performed on 15-s/30-frame standard trajectories: normalized radial position (0-1) and absolute distance from the cell border (μm).

Normalized radial position (0-1): To quantify the spatial positioning of particles within cells that are not necessarily circular, we implemented a normalized radial metric ranging from 0 to 1. This metric represents the particle's relative position along a line from the nucleus to the cell periphery, allowing for consistent spatial quantification across varying cell shapes. The nuclear boundary was defined as 0, while the periphery was set at 1. Each particle's position was then projected onto this radial axis based on its distance from the nucleus, normalized by the maximum distance between the nucleus and periphery. This approach facilitated spatial comparisons by expressing each particle's location as a fraction of the distance from the nuclear center, enabling a standardized measure of radial distribution even in irregularly shaped cells.

Absolute distance from the cell border (μm): To determine the absolute distance from the cell border, we calculated the shortest distance from each particle's position to the cell border, regardless of the cellular shape. To achieve this, we used the binary mask of the cytoplasmic mask, which defined the cell border to calculate the distances: fraction of trajectories displacing >1 μm versus radial position; and maximum displacement versus radial position heatmaps for immotile tracks (<1 μm) versus motile tracks (>1 μm).

FIB-SEM sample preparation, embedding, and imaging

COS-7 cells (CRL-1651; ATCC) were cultured on sapphire coverslips and subjected to HPF using a Wohlwend HPF Compact 02 machine. HPF was immediately followed by freeze substitution in media containing 2% osmium tetroxide, 0.1% uranyl acetate, and 3% water in acetone, performed in an automated freeze substitution system (AFS2; Leica Microsystems) with a controlled temperature ramp from −140°C to room temperature over 39 h. Subsequently, the samples were embedded in Durcupan ACM resin following a series of dehydration and infiltration steps and polymerized at 65°C for 48 h.

For FIB-SEM imaging, resin-embedded samples were trimmed to reveal the region of interest and sputter-coated with a dual layer of 10-nm gold followed by 100 nm carbon to enhance conductivity. Imaging was performed on a custom Zeiss FIB-SEM system equipped with a Zeiss Capella FIB column and a Gemini 500 SEM. The block face was sequentially imaged and milled using a focused gallium ion beam. The imaging was performed with a 250-pA electron beam with a landing energy of 0.9 keV and a pixel size of 2 nm, while the milling was conducted with a 15-nA gallium ion beam to remove 2 nm of material per cycle. This process was repeated continuously over 7 days to acquire a near-isotropic volumetric dataset.

FIB-SEM postprocessing

Following acquisition, the raw FIB-SEM image data underwent postprocessing steps including field flattening to compensate for nonuniform detector sensitivity and signal fusion to integrate data from secondary electron and backscattered electron detectors. Image registration and alignment were performed using a scale invariant feature transform algorithm with a regularized affine transformation model to ensure accurate reconstruction of the 3D volume.

3D reconstruction of filaments

Vimentin and MT trajectories were manually traced on either 2 or 4 nm isotropic voxel FIB-SEM volumes in KNOSSOS or WEBKNOSSOS. Using a custom Python script, XYZ trajectories for VIFs and MTs were extracted, linearly interpolated with uniform 4-nm sampling, and smoothed using the Savitzky–Golay filtering with a third-degree polynomial and window sizes of 55 points and 101 points for vimentin and MTs, respectively. For visualization, the coordinates of smoothed, interpolated trajectories were written to a JSON file and imported into Blender 4.2 using a custom Python script. In Blender, filaments were rendered as curve objects with a bevel depth equivalent to the filament radii as measured in the raw FIB-SEM dataset (6 nm for vimentin, 12 nm for MTs). For Video 7, a custom Python script was used to randomly pseudocolor the VIFs. All renders were generated using the Cycles render engine.

Online supplemental material

Fig. S1 shows sparse labeling of vimentin-SunTag in RPE cells. Fig. S2 shows endogenous vimentin organization is unaffected by vimentin-SunTag expression and exhibits co-mobility with dense vimentin-SunTag labeling. Fig. S3 shows SPT reveals complex VIF motility. Fig. S4 shows SPT analysis of vimentin-SunTag reveals equivalent rates of directed VIF motility across cellular regions. Fig. S5 shows vimentin briefly sustains its organization in the absence of MTs. Fig. S6 shows VIFs form loose bundle organization compared with keratin. Video 1 shows active transport of VIFs visualized by vimentin-SunTag. Video 2 shows endogenous VIF transport and organization are unaffected by vimentin-SunTag expression. Video 3 shows vimentin-SunTag reveals comparable VIF motility across cellular regions. Video 4 shows MT depolymerization inhibits long-range vimentin-SunTag movement. Video 5 shows kinesin-1 drives the long-range movement of vimentin-SunTag. Video 6 shows chemical inhibition of cytoplasmic dynein blocks vimentin-SunTag transport. Video 7 shows cytoplasmic dynein inhibition via p50 overexpression blocks vimentin-SunTag transport. Video 8 shows vimentin-SunTag trajectories align with MTs. Video 9 shows fly-through of a perinuclear FIB-SEM volume containing a VIF bundle. Video 10 shows 3D reconstruction of VIFs identified and tracked from the perinuclear FIB-SEM volume indicated in Fig. 7 A. Video 11 shows 3D reconstruction of perinuclear VIFs color-coded by average relative orientation. Video 12 shows 3D reconstruction of the perinuclear VIFs (blue) and MTs (white) reconstructed from the FIB-SEM volume. Video 13 shows 3D reconstruction comparing both perinuclear and peripheral reconstructions.

Data availability

All data reported in this paper will be shared upon reasonable request.

Acknowledgments

The authors thank Dr. Stephen A. Adam (Northwestern University) for stimulating discussions and critical reading of the manuscript, and Dr. Farida Korobova, Center for Advanced Microscopy (Northwestern University), for PREM sample preparation and EM image acquisition. W.-H. Yeo thanks the Christina Enroth-Cugell and David Cugell Fellowship for Visual Neuroscience and Biomedical Engineering at Northwestern University for their support.

The Gelfand laboratory is supported by the grant 2R35-GM131752 from the National Institute of General Medical Sciences. The Jennifer Lippincott-Schwartz laboratory is supported by the Howard Hughes Medical Institute Janelia Research Campus. H.F. Zhang acknowledges National Institutes of Health grants R01GM139151, R01GM140478, and U54CA268084.

Author contributions: B. Renganathan: conceptualization, data curation, formal analysis, investigation, methodology, project administration, resources, supervision, validation, visualization, and writing—original draft, review, and editing. A.S. Moore: conceptualization, formal analysis, investigation, software, visualization, and writing—original draft, review, and editing. W.-H. Yeo: formal analysis, methodology, visualization, and writing—review and editing. A. Petruncio: visualization. D. Ackerman: formal analysis. A.V. Weigel: data curation and software. The CellMap Team: data curation, resources, and software. H.A. Pasolli: investigation, methodology, validation, and writing—review and editing. C.S. Xu: data curation, formal analysis, methodology, software, and validation. G. Shtengel: investigation. H.F. Hess: methodology and project administration. A.S. Serpinskaya: investigation. H.F. Zhang: data curation, funding acquisition, investigation, methodology, resources, software, supervision, visualization, and writing—review and editing. J. Lippincott-Schwartz: supervision and writing—review and editing. V.I. Gelfand: conceptualization, formal analysis, funding acquisition, investigation, project administration, supervision, and writing—review and editing.

Disclosures: All authors have completed and submitted the ICMJE Form for Disclosure of Potential Conflicts of Interest. C.S. Xu reported a patent to US Patent 10,600,615 issued. No other disclosures were reported.

Submitted: 11 June 2024
Revised: 22 November 2024
Accepted: 9 January 2025

References

Barlan, K., M.J. Rossow, and V.I. Gelfand. 2013. The journey of the organelle: Teamwork and regulation in intracellular transport. *Curr. Opin. Cell Biol.* 25:483–488. https://doi.org/10.1016/j.ceb.2013.02.018

Bharathan, N.K., W. Giang, C.L. Hoffman, J.S. Aaron, S. Khuon, T.-L. Chew, S. Preibisch, E.T. Trautman, L. Heinrich, J. Bogovic, et al. 2023. Architecture and dynamics of a desmosome-endoplasmic reticulum complex. *Nat. Cell Biol.* 25:823–835. https://doi.org/10.1038/s41556-023-01154-4

Biskou, O., V. Casanova, K.M. Hooper, S. Kemp, G.P. Wright, J. Satsangi, P.G. Barlow, and C. Stevens. 2019. The type III intermediate filament vimentin regulates organelle distribution and modulates autophagy. *PLoS One*. 14:e0209665. https://doi.org/10.1371/journal.pone.0209665

Bomont, P. 2021. The dazzling rise of neurofilaments: Physiological functions and roles as biomarkers. *Curr. Opin. Cell Biol.* 68:181–191. https://doi.org/10.1016/j.ceb.2020.10.011

Brennich, M.E., S. Bauch, U. Vainio, T. Wedig, H. Herrmann, and S. Köster. 2014. Impact of ion valency on the assembly of vimentin studied by quantitative small angle X-ray scattering. *Soft Matter*. 10:2059–2068. https://doi.org/10.1039/C3SM52532E

Burgstaller, G., M. Gregor, L. Winter, and G. Wiche. 2010. Keeping the vimentin network under control: Cell-matrix adhesion-associated plectin 1f affects cell shape and polarity of fibroblasts. *Mol. Biol. Cell.* 21: 3362–3375. https://doi.org/10.1091/mbc.e10-02-0094

Burkhardt, J.K., C.J. Echeverri, T. Nilsson, and R.B. Vallee. 1997. Overexpression of the dynamitin (p50) subunit of the dynactin complex disrupts dynein-dependent maintenance of membrane organelle distribution. *J. Cell Biol.* 139:469–484. https://doi.org/10.1083/jcb.139.2.469

Chang, L., K. Barlan, Y.H. Chou, B. Grin, M. Lakonishok, A.S. Serpinskaya, D.K. Shumaker, H. Herrmann, V.I. Gelfand, and R.D. Goldman. 2009. The dynamic properties of intermediate filaments during organelle transport. *J. Cell Sci.* 122:2914–2923. https://doi.org/10.1242/jcs.046789

Chang, L., and R.D. Goldman. 2004. Intermediate filaments mediate cytoskeletal crosstalk. *Nat. Rev. Mol. Cell Biol.* 5:601–613. https://doi.org/10.1038/nrm1438

Cheng, F., Y. Shen, P. Mohanasundaram, M. Lindström, J. Ivaska, T. Ny, and J.E. Eriksson. 2016. Vimentin coordinates fibroblast proliferation and keratinocyte differentiation in wound healing via TGF-β-Slug signaling. *Proc. Natl. Acad. Sci. USA*. 113:E4320–E4327. https://doi.org/10.1073/pnas.1519197113

Coelho-Rato, L.S., S. Parvanian, S. Andrs Salajkova, O. Medalia, and J.E. Eriksson. 2024. Intermediate filaments at a glance. *J. Cell Sci.* 137:jcs261386. https://doi.org/10.1242/jcs.261386

Correia, I., D. Chu, Y.H. Chou, R.D. Goldman, and P. Matsudaira. 1999. Integrating the actin and vimentin cytoskeletons. adhesion-dependent formation of fimbrin-vimentin complexes in macrophages. *J. Cell Biol.* 146:831–842. https://doi.org/10.1083/jcb.146.4.831

Dean, K.M., P. Roudot, C.R. Reis, E.S. Welf, M. Mettlen, and R. Fiolka. 2016. Diagonally scanned light-sheet microscopy for fast volumetric imaging of adherent cells. *Biophys. J.* 110:1456–1465. https://doi.org/10.1016/j.bpj.2016.01.029

D'Souza, A.I., R. Grover, G.A. Monzon, L. Santen, and S. Diez. 2022. Vesicles driven by dynein and kinesin exhibit directional reversals without external regulators. *bioRxiv*. https://doi.org/10.1038/s41467-023-42605-8 (Preprint posted September 28, 2022).

Eckes, B., E. Colucci-Guyon, H. Smola, S. Nodder, C. Babinet, T. Krieg, and P. Martin. 2000. Impaired wound healing in embryonic and adult mice lacking vimentin. *J. Cell Sci.* 113:2455–2462. https://doi.org/10.1242/jcs.113.13.2455

Eibauer, M., M.S. Weber, R. Kronenberg-Tenga, C.T. Beales, R. Boujemaa-Paterski, Y. Turgay, S. Sivagurunathan, J. Kraxner, S. Köster, R.D. Goldman, and O. Medalia. 2024. Vimentin filaments integrate low-complexity domains in a complex helical structure. *Nat. Struct. Mol. Biol.* 31:939–949. https://doi.org/10.1038/s41594-024-01261-2

Esue, O., A.A. Carson, Y. Tseng, and D. Wirtz. 2006. A direct interaction between actin and vimentin filaments mediated by the tail domain of vimentin. *J. Biol. Chem.* 281:30393–30399. https://doi.org/10.1074/jbc.M605452200

Evans, R.D., C. Robinson, D.A. Briggs, D.J. Tooth, J.S. Ramalho, M. Cantero, L. Montoliu, S. Patel, E.V. Sviderskaya, and A.N. Hume. 2014. Myosin-Va and dynamic actin oppose microtubules to drive long-range organelle transport. *Curr. Biol.* 24:1743–1750. https://doi.org/10.1016/j.cub.2014.06.019

Franke, W.W., E. Schmid, M. Osborn, and K. Weber. 1978. Different intermediate-sized filaments distinguished by immunofluorescence microscopy. *Proc. Natl. Acad. Sci. USA*. 75:5034–5038. https://doi.org/10.1073/pnas.75.10.5034

Gan, Z., L. Ding, C.J. Burckhardt, J. Lowery, A. Zaritsky, K. Sitterley, A. Mota, N. Costigliola, C.G. Starker, D.F. Voytas, et al. 2016. Vimentin intermediate filaments template microtubule networks to enhance persistence in cell polarity and directed migration. *Cell Syst.* 3:252–263.e8. https://doi.org/10.1016/j.cels.2016.08.007

Gyoeva, F.K., and V.I. Gelfand. 1991. Coalignment of vimentin intermediate filaments with microtubules depends on kinesin. *Nature*. 353:445–448. https://doi.org/10.1038/353445a0

Helfand, B.T., A. Mikami, R.B. Vallee, and R.D. Goldman. 2002. A requirement for cytoplasmic dynein and dynactin in intermediate filament network assembly and organization. *J. Cell Biol.* 157:795–806. https://doi.org/10.1083/jcb.200202027

Hendricks, A.G., E. Perlson, J.L. Ross, H.W. Schroeder III, M. Tokito, and E.L.F. Holzbaur. 2010. Motor coordination via a tug-of-war mechanism drives bidirectional vesicle transport. *Curr. Biol.* 20:697–702. https://doi.org/10.1016/j.cub.2010.02.058

Herrmann, H., and U. Aebi. 2004. Intermediate filaments: Molecular structure, assembly mechanism, and integration into functionally distinct intracellular scaffolds. *Annu. Rev. Biochem.* 73:749–789. https://doi.org/10.1146/annurev.biochem.73.011303.073823

Herrmann, H., H. Bär, L. Kreplak, S.V. Strelkov, and U. Aebi. 2007. Intermediate filaments: From cell architecture to nanomechanics. *Nat. Rev. Mol. Cell Biol.* 8:562–573. https://doi.org/10.1038/nrm2197

Ho, C.-L., J.L. Martys, A. Mikhailov, G.G. Gundersen, and R.K.H Liem. 1998. Novel features of intermediate filament dynamics revealed by green fluorescent protein chimeras. *J. Cell Sci.* 111:1767–1778. https://doi.org/10.1242/jcs.111.13.1767

Hollenbeck, P.J., A.D. Bershadsky, O.Y. Pletjushkina, I.S. Tint, and J.M. Vasiliev. 1989. Intermediate filament collapse is an ATP-dependent and actin-dependent process. *J. Cell Sci.* 92:621–631. https://doi.org/10.1242/jcs.92.4.621

Hookway, C., L. Ding, M.W. Davidson, J.Z. Rappoport, G. Danuser, and V.I. Gelfand. 2015. Microtubule-dependent transport and dynamics of vimentin intermediate filaments. *Mol. Biol. Cell.* 26:1675–1686. https://doi.org/10.1091/mbc.E14-09-1398

Hu, J., Y. Li, Y. Hao, T. Zheng, S.K. Gupta, G.A. Parada, H. Wu, S. Lin, S. Wang, X. Zhao, et al. 2019. High stretchability, strength, and toughness of living cells enabled by hyperelastic vimentin intermediate filaments. *Proc. Natl. Acad. Sci. USA*. 116:17175–17180. https://doi.org/10.1073/pnas.1903890116

Ishikawa, H., R. Bischoff, and H. Holtzer. 1968. Mitosis and intermediate-sized filaments in developing skeletal muscle. *J. Cell Biol.* 38:538–555. https://doi.org/10.1083/jcb.38.3.538

Janmey, P.A., U. Euteneuer, P. Traub, and M. Schliwa. 1991. Viscoelastic properties of vimentin compared with other filamentous biopolymer networks. *J. Cell Biol.* 113:155–160. https://doi.org/10.1083/jcb.113.1.155

Jaqaman, K., D. Loerke, M. Mettlen, H. Kuwata, S. Grinstein, S.L. Schmid, and G. Danuser. 2008. Robust single-particle tracking in live-cell time-lapse sequences. *Nat. Methods*. 5:695–702. https://doi.org/10.1038/nmeth.1237

Kim, H., F. Nakamura, W. Lee, Y. Shifrin, P. Arora, and C.A. McCulloch. 2010. Filamin A is required for vimentin-mediated cell adhesion and spreading. *Am. J. Physiol. Cell Physiol.* 298:C221–C236. https://doi.org/10.1152/ajpcell.00323.2009

Kim, S., and P.A. Coulombe. 2007. Intermediate filament scaffolds fulfill mechanical, organizational, and signaling functions in the cytoplasm. *Genes Dev.* 21:1581–1597. https://doi.org/10.1101/gad.1552107

Korobova, F., and T. Svitkina. 2008. Arp2/3 complex is important for filopodia formation, growth cone motility, and neuritogenesis in neuronal cells. *Mol. Biol. Cell.* 19:1561–1574. https://doi.org/10.1091/mbc.e07-09-0964

Kural, C., H. Kim, S. Syed, G. Goshima, V.I. Gelfand, and P.R. Selvin. 2005. Kinesin and dynein move a peroxisome in vivo: A tug-of-war or coordinated movement? *Science*. 308:1469–1472. https://doi.org/10.1126/science.1108408

Langford, G.M. 1995. Actin- and microtubule-dependent organelle motors: Interrelationships between the two motility systems. *Curr. Opin. Cell Biol.* 7:82–88. https://doi.org/10.1016/0955-0674(95)80048-4

Lazarides, E. 1982. Intermediate filaments: A chemically heterogeneous, developmentally regulated class of proteins. *Annu. Rev. Biochem.* 51: 219–250. https://doi.org/10.1146/annurev.bi.51.070182.001251

Linkert, M., C.T. Rueden, C. Allan, J.M. Burel, W. Moore, A. Patterson, B. Loranger, J. Moore, C. Neves, D. Macdonald, et al. 2010. Metadata matters: Access to image data in the real world. *J. Cell Biol.* 189:777–782. https://doi.org/10.1083/jcb.201004104

Lowery, J., E.R. Kuczmarski, H. Herrmann, and R.D. Goldman. 2015. Intermediate filaments play a pivotal role in regulating cell architecture and function. *J. Biol. Chem.* 290:17145–17153. https://doi.org/10.1074/jbc.R115.640359

Lynch, C.D., A.M. Lazar, T. Iskratsch, X. Zhang, and M.P. Sheetz. 2013. Endoplasmic spreading requires coalescence of vimentin intermediate filaments at force-bearing adhesions. *Mol. Biol. Cell.* 24:21–30. https://doi.org/10.1091/mbc.e12-05-0377

Mack, J.W., A.C. Steven, and P.M. Steinert. 1993. The mechanism of interaction of filaggrin with intermediate filaments. The ionic zipper hypothesis. *J. Mol. Biol.* 232:50–66. https://doi.org/10.1006/jmbi.1993.1369

Miura, K. 2020. Bleach correction ImageJ plugin for compensating the photobleaching of time-lapse sequences. *F1000 Res.* 9:1494. https://doi.org/10.12688/f1000research.27171.1

Mohan, A.S., K.M. Dean, T. Isogai, S.Y. Kasitinon, V.S. Murali, P. Roudot, A. Groisman, D.K. Reed, E.S. Welf, S.J. Han, et al. 2019. Enhanced dendritic actin network formation in extended lamellipodia drives proliferation in growth-challenged Rac1^{P29S} melanoma cells. *Dev. Cell.* 49:444–460.e9. https://doi.org/10.1016/j.devcel.2019.04.007

Nebl, T., K.N. Pestonjamasp, J.D. Leszyk, J.L. Crowley, S.W. Oh, and E.J. Luna. 2002. Proteomic analysis of a detergent-resistant membrane skeleton from neutrophil plasma membranes. *J. Biol. Chem.* 277:43399–43409. https://doi.org/10.1074/jbc.M205386200

Nekrasova, O.E., M.G. Mendez, I.S. Chernoivanenko, P.A. Tyurin-Kuzmin, E.R. Kuczmarski, V.I. Gelfand, R.D. Goldman, and A.A. Minin. 2011. Vimentin intermediate filaments modulate the motility of mitochondria. *Mol. Biol. Cell.* 22:2282–2289. https://doi.org/10.1091/mbc.e10-09-0766

Omary, M.B., P.A. Coulombe, and W.H.I. McLean. 2004. Intermediate filament proteins and their associated diseases. *N. Engl. J. Med.* 351: 2087–2100. https://doi.org/10.1056/NEJMra040319

Ovesný, M., P. Křížek, J. Borkovec, Z. Švindrych, and G.M. Hagen. 2014. ThunderSTORM: A comprehensive ImageJ plug-in for PALM and STORM data analysis and super-resolution imaging. *Bioinformatics.* 30:2389–2390. https://doi.org/10.1093/bioinformatics/btu202

Pallari, H.M., and J.E. Eriksson. 2006. Intermediate filaments as signaling platforms. *Sci. STKE.* 2006:pe53. https://doi.org/10.1126/stke.3662006pe53

Patteson, A.E., A. Vahabikashi, K. Pogoda, S.A. Adam, K. Mandal, M. Kittisopikul, S. Sivagurunathan, A. Goldman, R.D. Goldman, and P.A. Janmey. 2019. Vimentin protects cells against nuclear rupture and DNA damage during migration. *J. Cell Biol.* 218:4079–4092. https://doi.org/10.1083/jcb.201902046

Perlson, E., S. Hanz, K. Ben-Yaakov, Y. Segal-Ruder, R. Seger, and M. Fainzilber. 2005. Vimentin-dependent spatial translocation of an activated MAP kinase in injured nerve. *Neuron.* 45:715–726. https://doi.org/10.1016/j.neuron.2005.01.023

Pogoda, K., F. Byfield, P. Deptuła, M. Cieśluk, Ł. Suprewicz, K. Skłodowski, J.L. Shivers, A. van Oosten, K. Cruz, E. Tarasovetc, et al. 2022. Unique role of vimentin networks in compression stiffening of cells and protection of nuclei from compressive stress. *Nano Lett.* 22:4725–4732. https://doi.org/10.1021/acs.nanolett.2c00736

Pogoda, K., and P.A. Janmey. 2023. Transmit and protect: The mechanical functions of intermediate filaments. *Curr. Opin. Cell Biol.* 85:102281. https://doi.org/10.1016/j.ceb.2023.102281

Portet, S., N. Mücke, R. Kirmse, J. Langowski, M. Beil, and H. Herrmann. 2009. Vimentin intermediate filament formation: In vitro measurement and mathematical modeling of the filament length distribution during assembly. *Langmuir.* 25:8817–8823. https://doi.org/10.1021/la900509r

Pradeau-Phélut, L., and S. Etienne-Manneville. 2024. Cytoskeletal crosstalk: A focus on intermediate filaments. *Curr. Opin. Cell Biol.* 87:102325. https://doi.org/10.1016/j.ceb.2024.102325

Prahlad, V., M. Yoon, R.D. Moir, R.D. Vale, and R.D. Goldman. 1998. Rapid movements of vimentin on microtubule tracks: Kinesin-dependent assembly of intermediate filament networks. *J. Cell Biol.* 143:159–170. https://doi.org/10.1083/jcb.143.1.159

Redmond, C.J., and P.A. Coulombe. 2021. Intermediate filaments as effectors of differentiation. *Curr. Opin. Cell Biol.* 68:155–162. https://doi.org/10.1016/j.ceb.2020.10.009

Renganathan, B., J.P. Zewe, Y. Cheng, J.M. Paumier, M. Kittisopikul, K.M. Ridge, P. Opal, and V.I. Gelfand. 2023. Gigaxonin is required for intermediate filament transport. *FASEB J.* 37:e22886. https://doi.org/10.1096/fj.202202119R

Robert, A., C. Hookway, and V.I. Gelfand. 2016. Intermediate filament dynamics: What we can see now and why it matters. *BioEssays.* 38: 232–243. https://doi.org/10.1002/bies.201500142

Robert, A., P. Tian, S.A. Adam, M. Kittisopikul, K. Jaqaman, R.D. Goldman, and V.I. Gelfand. 2019. Kinesin-dependent transport of keratin filaments: A unified mechanism for intermediate filament transport. *FASEB J.* 33: 388–399. https://doi.org/10.1096/fj.201800604R

Rogers, S.L., and V.I. Gelfand. 1998. Myosin cooperates with microtubule motors during organelle transport in melanophores. *Curr. Biol.* 8: 161–164. https://doi.org/10.1016/S0960-9822(98)70063-6

Schaedel, L., C. Lorenz, A.V. Schepers, S. Klumpp, and S. Köster. 2021. Vimentin intermediate filaments stabilize dynamic microtubules by direct interactions. *Nat. Commun.* 12:3799. https://doi.org/10.1038/s41467-021-23523-z

Schindelin, J., I. Arganda-Carreras, E. Frise, V. Kaynig, M. Longair, T. Pietzsch, S. Preibisch, C. Rueden, S. Saalfeld, B. Schmid, et al. 2012. Fiji: An open-source platform for biological-image analysis. *Nat. Methods.* 9: 676–682. https://doi.org/10.1038/nmeth.2019

Schwarz, N., and R.E. Leube. 2016. Intermediate filaments as organizers of cellular space: How they affect mitochondrial structure and function. *Cells.* 5:30. https://doi.org/10.3390/cells5030030

Seetharaman, S., and S. Etienne-Manneville. 2020. Cytoskeletal crosstalk in cell migration. *Trends Cell Biol.* 30:720–735. https://doi.org/10.1016/j.tcb.2020.06.004

Shen, Y., H. Wu, P.J. Lu, D. Wang, M. Shayegan, H. Li, W. Shi, Z. Wang, L.H. Cai, J. Xia, et al. 2021. Effects of vimentin intermediate filaments on the structure and dynamics of in vitro multicomponent interpenetrating cytoskeletal networks. *Phys. Rev. Lett.* 127:108101. https://doi.org/10.1103/PhysRevLett.127.108101

Simon, F., L.E. Weiss, and S. van Teeffelen. 2024. A guide to single-particle tracking. *Nat. Rev. Methods Primers.* 4:66. https://doi.org/10.1038/s43586-024-00341-3

Starger, J.M., W.E. Brown, A.E. Goldman, and R.D. Goldman. 1978. Biochemical and immunological analysis of rapidly purified 10-nm filaments from baby hamster kidney (BHK-21) cells. *J. Cell Biol.* 78:93–109. https://doi.org/10.1083/jcb.78.1.93

Steinert, P.M., A.C. Steven, and D.R. Roop. 1985. The molecular biology of intermediate filaments. *Cell.* 42:411–420. https://doi.org/10.1016/0092-8674(85)90098-4

Svitkina, T. 2009. Imaging cytoskeleton components by electron microscopy. *Methods Mol. Biol.* 586:187–206. https://doi.org/10.1007/978-1-60761-376-3_10

Szeverenyi, I., A.J. Cassidy, C.W. Chung, B.T.K. Lee, J.E.A. Common, S.C. Ogg, H. Chen, S.Y. Sim, W.L.P. Goh, K.W. Ng, et al. 2008. The human Intermediate filament database: Comprehensive information on a gene family involved in many human diseases. *Hum. Mutat.* 29:351–360. https://doi.org/10.1002/humu.20652

Tanenbaum, M.E., L.A. Gilbert, L.S. Qi, J.S. Weissman, and R.D. Vale. 2014. A protein-tagging system for signal amplification in gene expression and fluorescence imaging. *Cell.* 159:635–646. https://doi.org/10.1016/j.cell.2014.09.039

Vale, R.D. 2003. The molecular motor toolbox for intracellular transport. *Cell.* 112:467–480. https://doi.org/10.1016/S0092-8674(03)00111-9

Vikstrom, K.L., S.S. Lim, R.D. Goldman, and G.G. Borisy. 1992. Steady state dynamics of intermediate filament networks. *J. Cell Biol.* 118:121–129. https://doi.org/10.1083/jcb.118.1.121

Vitali, T., R. Sanchez-Alvarez, T.M. Witkos, I. Bantounas, M.F.A. Cutiongco, M. Dudek, G. Yan, A.A. Mironov, J. Swift, and M. Lowe. 2023. Vimentin intermediate filaments provide structural stability to the mammalian Golgi complex. *J. Cell Sci.* 136:jcs260577. https://doi.org/10.1242/jcs.260577

Windoffer, R., N. Schwarz, S. Yoon, T. Piskova, M. Scholkemper, J. Stegmaier, A. Bönsch, J. Di Russo, and R.E. Leube. 2022. Quantitative mapping of keratin networks in 3D. *Elife.* 11:e75894. https://doi.org/10.7554/eLife.75894

Winheim, S., A.R. Hieb, M. Silbermann, E.M. Surmann, T. Wedig, H. Herrmann, J. Langowski, and N. Mücke. 2011. Deconstructing the late phase of vimentin assembly by total internal reflection fluorescence microscopy (TIRFM). *PLoS One.* 6:e19202. https://doi.org/10.1371/journal.pone.0019202

Wu, H., Y. Shen, S. Sivagurunathan, M.S. Weber, S.A. Adam, J.H. Shin, J.J. Fredberg, O. Medalia, R. Goldman, and D.A. Weitz. 2022. Vimentin intermediate filaments and filamentous actin form unexpected interpenetrating networks that redefine the cell cortex. *Proc. Natl. Acad. Sci. USA.* 119:e2115217119. https://doi.org/10.1073/pnas.2115217119

Wu, H., Y. Shen, D. Wang, H. Herrmann, R.D. Goldman, and D.A. Weitz. 2020. Effect of divalent cations on the structure and mechanics of vimentin intermediate filaments. *Biophys. J.* 119:55–64. https://doi.org/10.1016/j.bpj.2020.05.016

Xu, C.S., S. Pang, G. Shtengel, A. Müller, A.T. Ritter, H.K. Hoffman, S. ya Takemura, Z. Lu, H.A. Pasolli, N. Iyer, et al. 2021. An open-access volume electron microscopy atlas of whole cells and tissues. *Nature.* 599: 147–151. https://doi.org/10.1038/s41586-021-03992-4

Yoon, M., R.D. Moir, V. Prahlad, and R.D. Goldman. 1998. Motile properties of vimentin intermediate filament networks in living cells. *J. Cell Biol.* 143: 147–157. https://doi.org/10.1083/jcb.143.1.147

Supplemental material

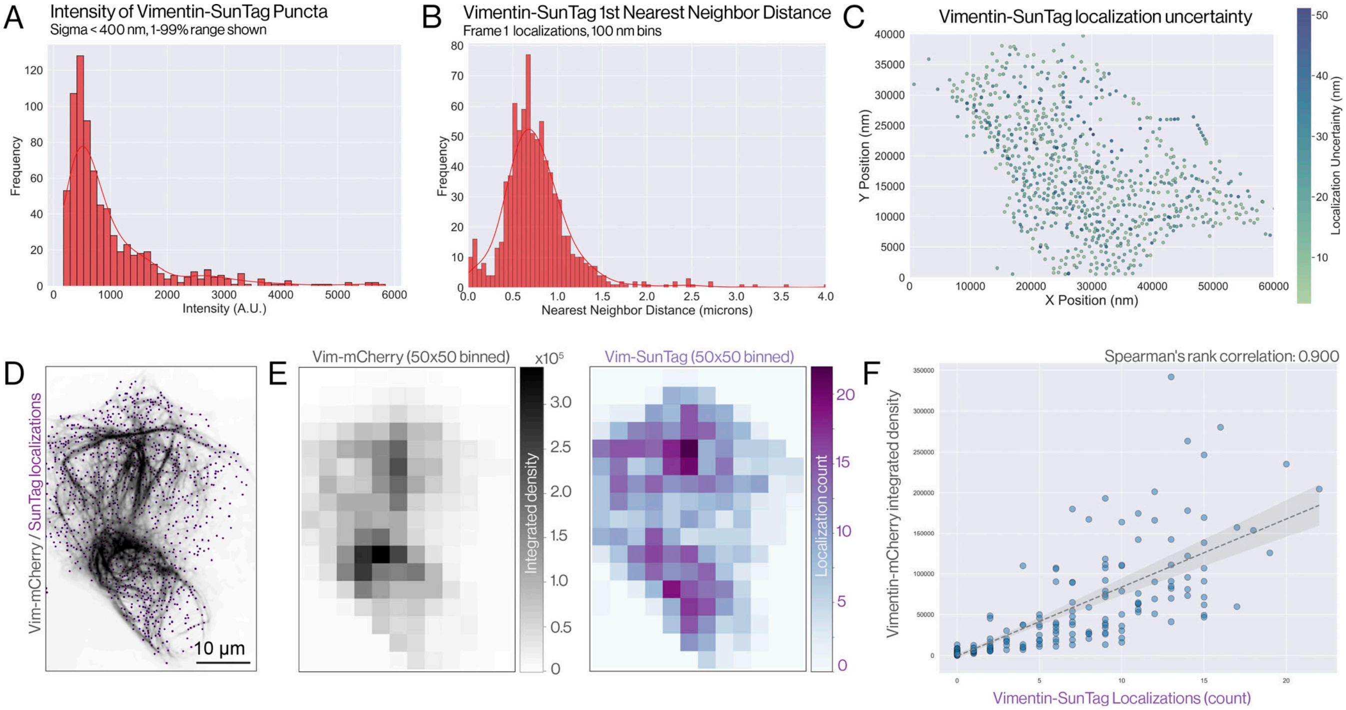

Figure S1. **Sparse labeling of vimentin-SunTag in RPE cells. (A)** Frequency distribution of fluorescence intensity among detected SunTag particles in a control RPE. **(B)** Frequency distribution of first NND (microns) between detected SunTag particles in the same cell. **(C)** Spatial map of vimentin-SunTag localizations, pseudocolored by localization uncertainty (nm) of our fits. **(D)** Spinning disk confocal micrograph of an RPE cell co-transfected with vimentin-mCherry and vimentin-SunTag (from Fig. 1 B). The ensemble vimentin-mCherry signal is displayed in black, with SunTag localizations overlaid as purple spots. **(E)** 50 × 50 pixel binned heatmaps of vimentin-mCherry integrated density (left, black) and vimentin-SunTag particle count (right, purple). **(F)** Scatter plot indicating density of vimentin-mCherry relative to vimentin-SunTag particle detection in each 50 × 50 bin. Spearman's rank correlation = 0.900.

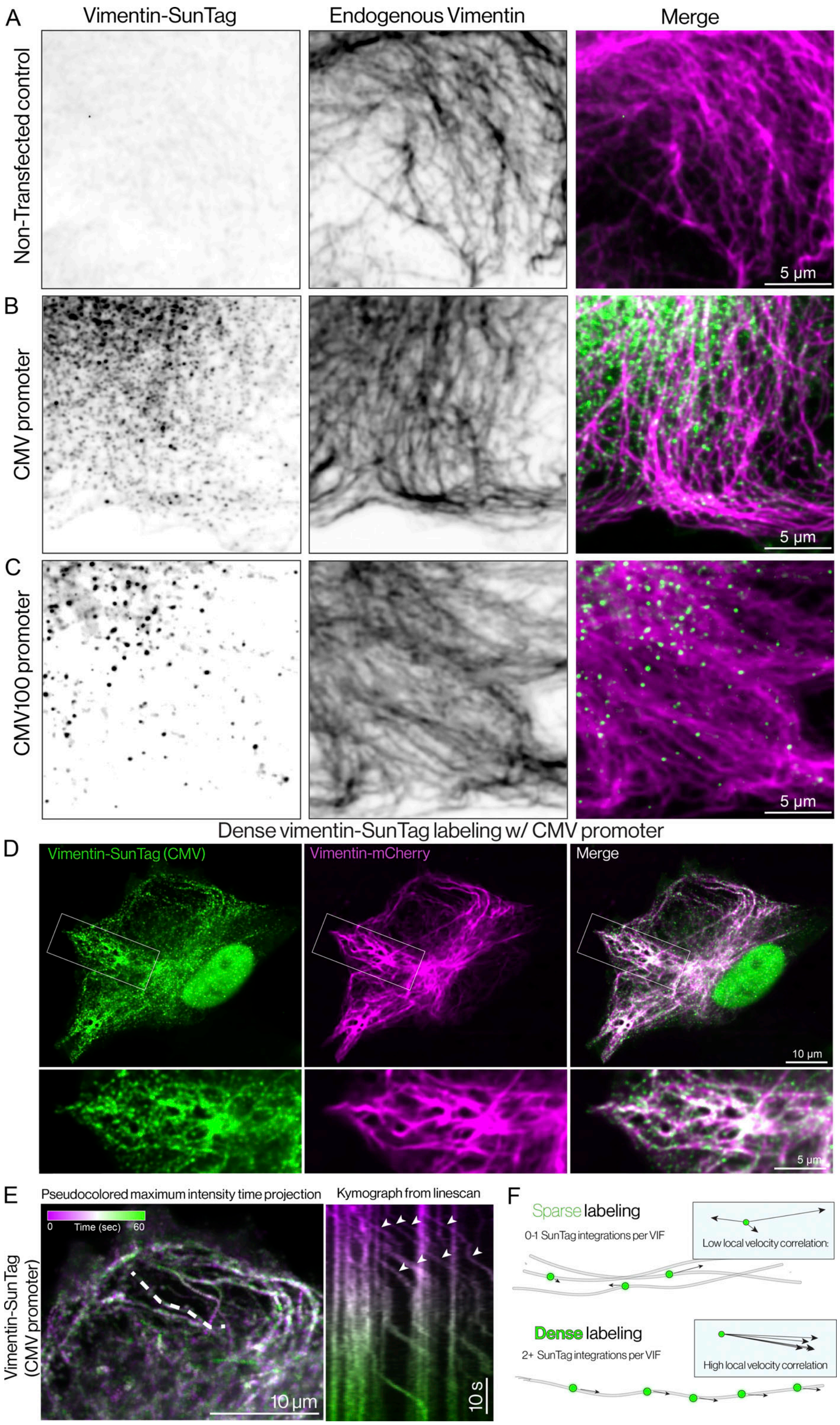

Figure S2. **Endogenous vimentin organization is unaffected by vimentin-SunTag expression and exhibits co-mobility with dense vimentin-SunTag labeling. (A–C)** Representative spinning disk confocal micrographs of fixed RPE cells showing immunostained vimentin and either (A) empty GFP channel in a nontransfected control, (B) vimentin-SunTag expressed under the standard full-length CMV promoter, or (C) vimentin-SunTag expressed under the truncated, inefficient CMV100 promoter. **(D)** RPE cells transfected with standard full-length CMV-vimentin-SunTag (green) and vimentin-mCherry (magenta), a snapshot from the time-lapse image (see Video 2). Inset indicates a region of highly saturated vimentin-SunTag labeling density, complicating efforts to localize single particles. **(E)** Pseudocolored maximum intensity time projection of dense-labeled vimentin-SunTag particles over 121 frames (60 s). The dashed line indicates the position of the line scan used to generate kymograph (right). Arrows indicate SunTag trajectories with both uniform velocity and constant relative spacing, a motility pattern consistent with multiple spots associated with a single motile filament. **(F)** Cartoon indicating predicted vimentin-SunTag local motility in either sparse (top) or dense (bottom) labeling regimes.

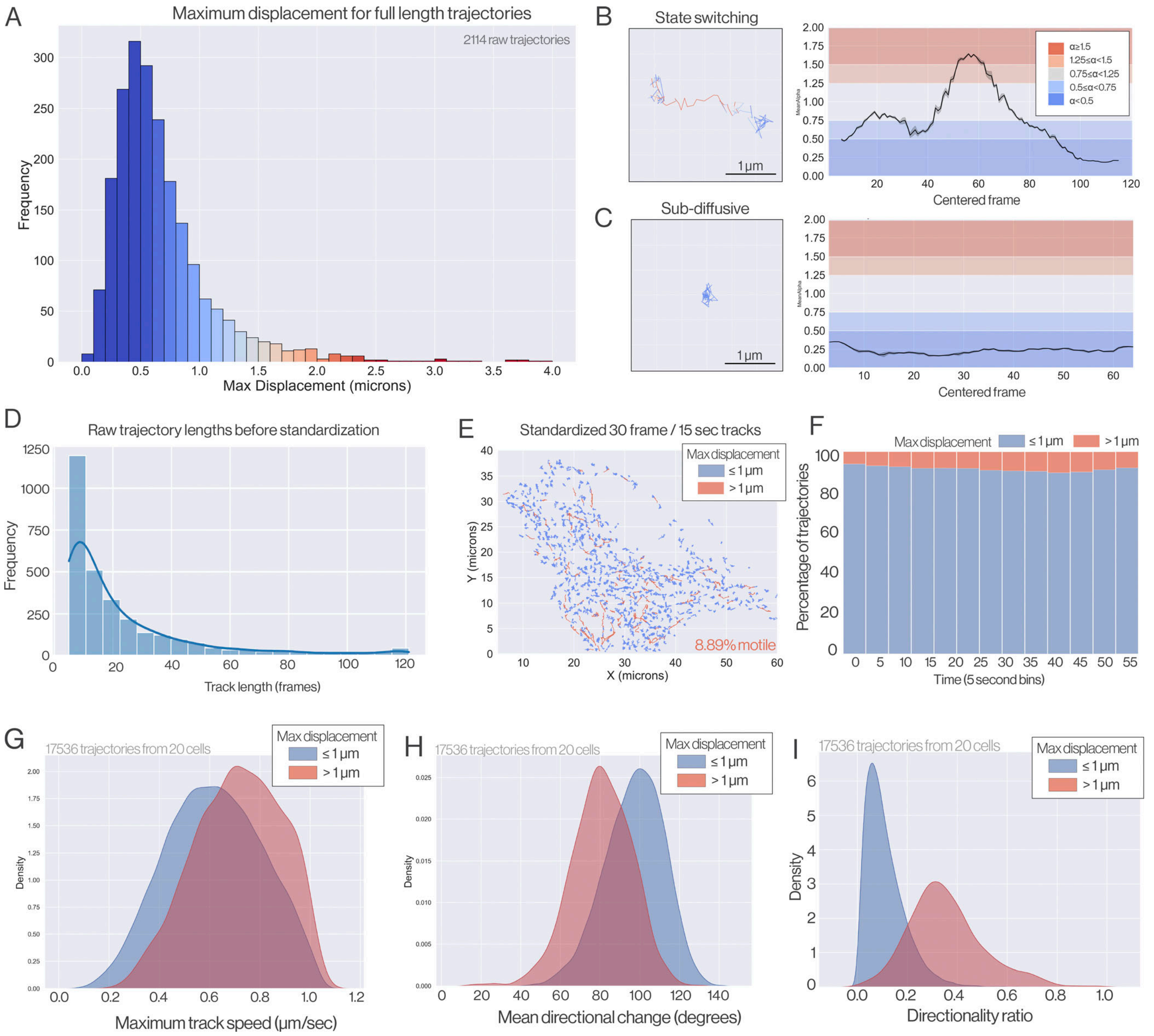

Figure S3. **SPT reveals complex VIF motility. (A)** Frequency distribution of maximum displacements for full-length trajectories shown in Fig. 2 B. **(B and C)** Color-coded trajectories and accompanying plots of alpha values computed from 20-frame sliding window MSD analyses centered at the indicated frames. **(B)** Trajectory that undergoes clear motility state transitions. **(C)** Highly confined trajectory that remains subdiffusive for the entire trajectory. **(D)** Frequency distribution with the kernel density estimate of raw trajectory lengths from the cell shown in Fig. 2 B. **(E)** Standardized 30-frame SPT trajectories of vimentin-SunTag spots in a single RPE cell over 1 min. Trajectories have been color-coded based on maximum displacement according to the legend. **(F)** Percentage of standardized vimentin-SunTag trajectories classified as motile (red) or immotile (blue) over consecutive, nonoverlapping 5-s bins from a 1-min movie. X axis numbering indicates bin start times. **(G–I)** Kernel density estimate plots indicating distribution of maximum track speeds (G), mean track directional change (H), and directionality ratio (I) for motile (blue) and immotile (red) standardized trajectories.

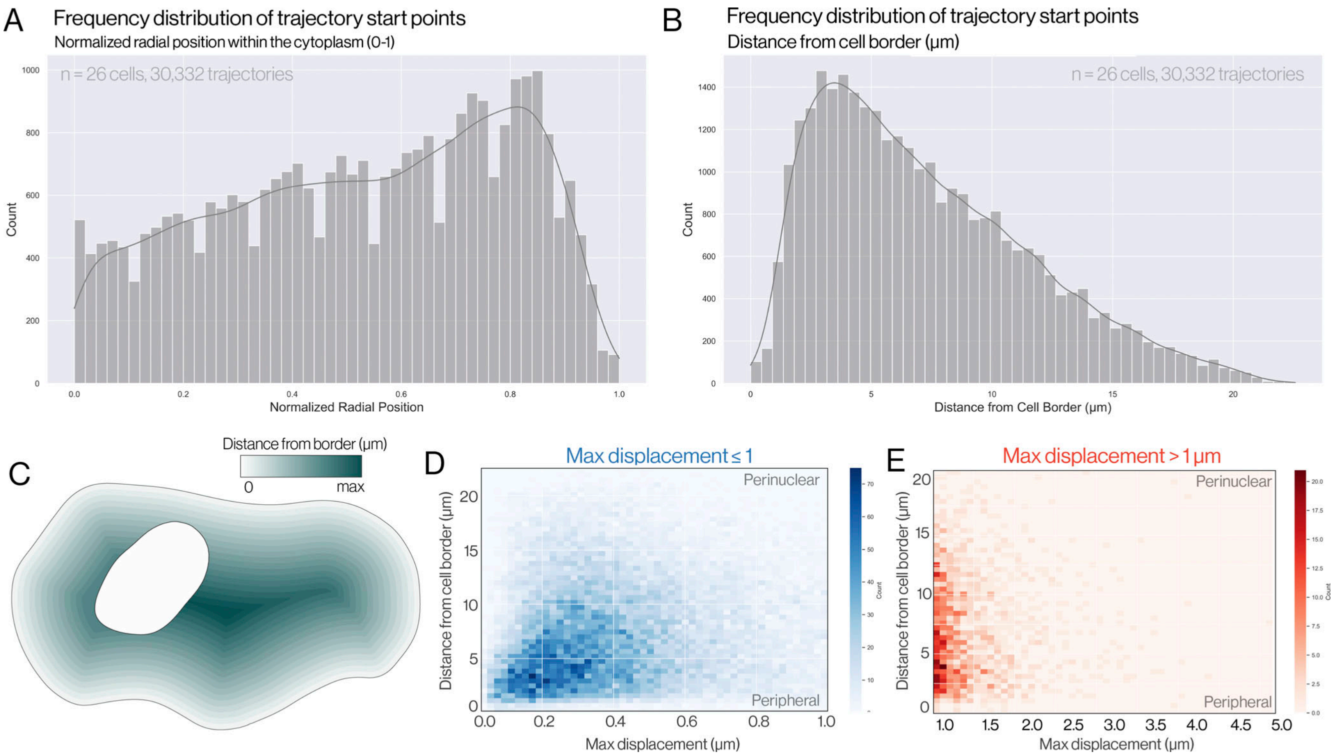

Figure S4. **SPT analysis of vimentin-SunTag reveals equivalent rates of directed VIF motility across cellular regions. (A and B)** Frequency distribution of track start positions mapped according to (A) normalized radial position, wherein the nuclear envelope = 0 and the edge of the cell = 1 or (B) distance from cell border in microns. 30,332 trajectories were analyzed, derived from 26 cells. The kernel density estimate is shown as a superimposed line. **(C)** Schematic indicating spatial mapping used to calculate the distance from the border. **(D and E)** 2D histograms plotting the initial distance from the cell border and final maximum displacement for either immotile (D) or motile (E) 15-s trajectories.

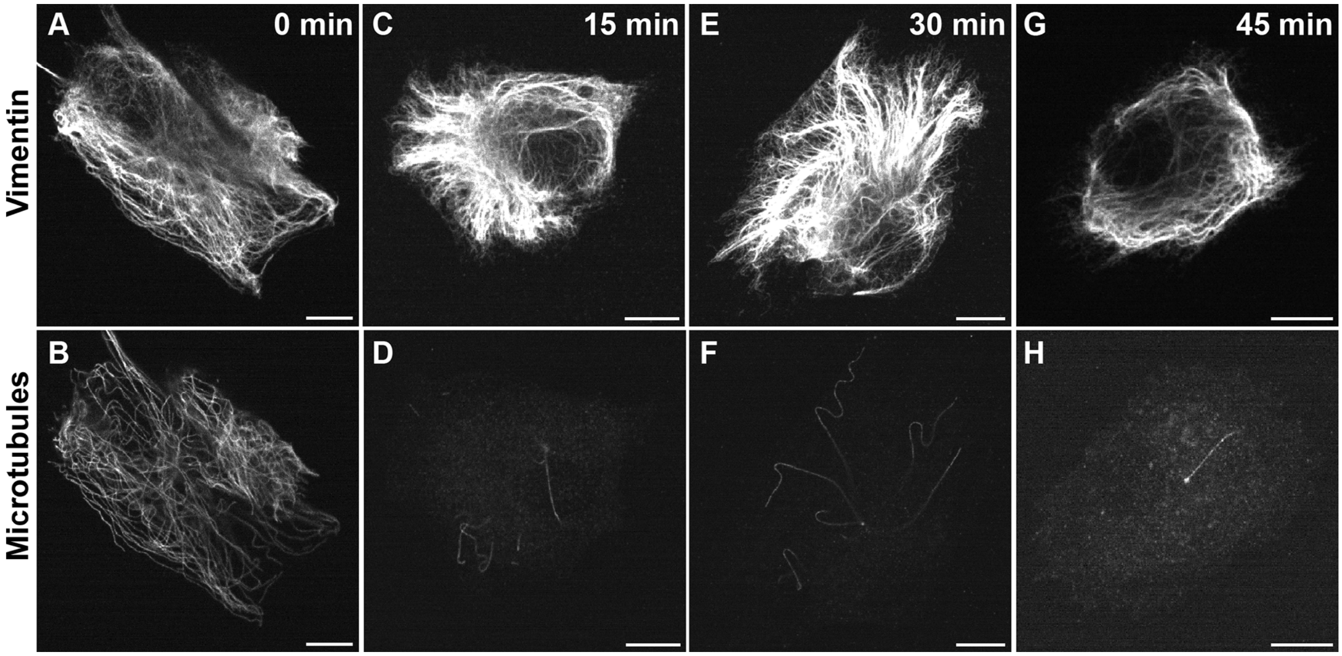

Figure S5. **Vimentin briefly sustains its organization in the absence of MTs.** RPE cells were treated with 10 µM nocodazole for various time points. Subsequently, the cells were fixed and stained for vimentin and MTs. The upper panel depicts the organization of vimentin at different time points following nocodazole treatment. The bottom panel displays the corresponding MT staining for the respective cells. Scale bar: 10 µm.

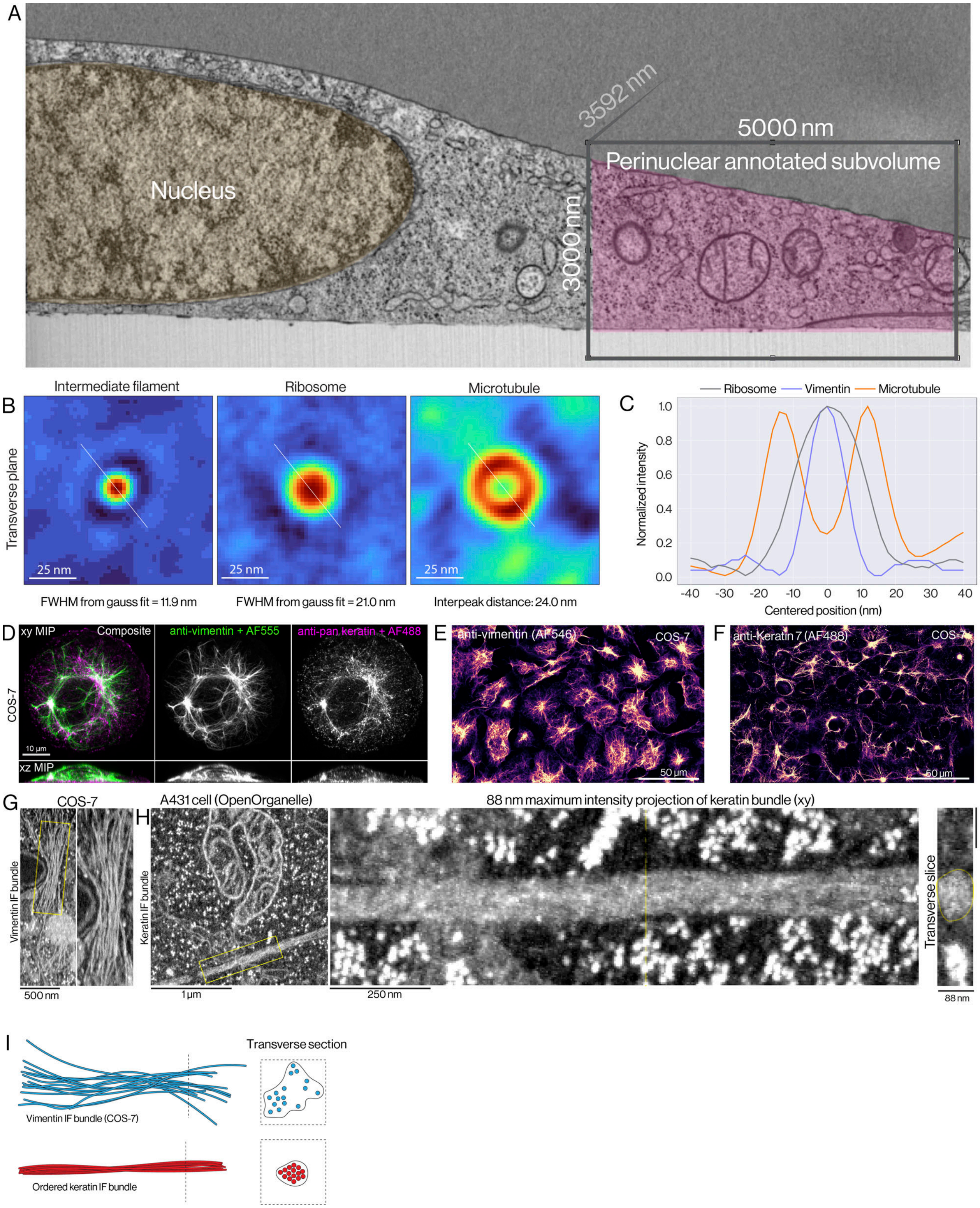

Figure S6. **VIFs form loose bundle organization compared with keratin. (A)** FIB-SEM slice indicating the position of analyzed subvolume presented in Fig. 7 A. **(B)** Center-aligned average projections of VIFs (left), ribosomes (center), and MTs (right) with the measured size of each averaged structure indicated below. White diagonal lines indicate the position of the line profile used in C. **(C)** Intensity profile of averaged ribosome, vimentin, and MT profiles shown in C. Plots indicate mean intensity along each profile at 360 1° rotations. **(D)** Double immunolabeling of a COS-7 cell with anti-vimentin (green) and anti-pan-keratin (magenta) antibodies. **(E and F)** Immunolabeling of vimentin (E) and keratin 7 (F) in COS-7 cells across a large field of view. Images were collected and stitched together. In F, a stitching artifact is present due to sample drift between sequentially acquired volume tiles. **(G and H)** VIF bundles from COS-7 cells and (H) keratin bundles from A431 cells highlight the structural dissimilarity between them (source: https://openorganelle.janelia.org/datasets/aic_desmosome-3). **(I)** Cartoon representation illustrating the loose organization of vimentin bundles versus the highly ordered and compact structure of keratin bundles.

Video 1. **Active transport of VIFs visualized by vimentin-SunTag.** Cells co-express the ensemble vimentin reporter vimentin-mCherry (magenta) and sparsely labeled vimentin-SunTag (green), driven by the truncated, inefficient CMV100 promoter. The green dots correspond to dynamically transported vimentin-SunTag, reflecting the motility of VIFs. A zoomed-in view of the white-boxed region is included.

Video 2. **Endogenous VIF transport and organization are unaffected by vimentin-SunTag expression.** Cells co-express the ensemble vimentin reporter vimentin-mCherry (magenta) and sparsely labeled vimentin-SunTag (green), driven by the standard CMV promoter. A zoomed-in view of the white-boxed region highlights the co-mobility of multiple vimentin-SunTag particles along a single motile filament.

Video 3. **Vimentin-SunTag reveals comparable VIF motility across cellular regions.** Cells sparsely labeled with vimentin-SunTag show trajectories color-coded based on their maximum displacement (blue: ≤1 µm; red: >1 µm). Enlarged views of the perinuclear and peripheral regions are shown below.

Video 4. **MT depolymerization inhibits long-range vimentin-SunTag movement.** Cells treated with 10 µM nocodazole exhibit a significant reduction in the long trajectories of vimentin-SunTag particles. Trajectories are color-coded based on maximum displacement (blue: ≤1 µm; red: >1 µm).

Video 5. **Kinesin-1 drives long-range movement of vimentin-SunTag.** In kinesin-1–null cells, active vimentin-SunTag transport is abolished, with most particles clustering in the perinuclear region. Long, linear trajectories are absent, and most particles exhibit confined movement. Trajectories are color-coded based on maximum displacement (blue: ≤1 µm; red: >1 µm).

Video 6. **Chemical inhibition of cytoplasmic dynein blocks vimentin-SunTag transport.** Control cells treated with 5 µM dynapyrazole A exhibit a loss of long-range vimentin-SunTag transport and an increase in confined motility. Trajectories are color-coded based on maximum displacement (blue: ≤1 µm; red: >1 µm).

Video 7. **Cytoplasmic dynein inhibition via p50 overexpression blocks vimentin-SunTag transport.** Dynein inhibition through p50 overexpression leads to perinuclear accumulation of vimentin-SunTag, resembling the pattern observed in kinesin-1–null cells. Cytoplasmic dynein was inhibited by co-expressing dynamitin/p50 with vimentin-SunTag. Trajectories are color-coded based on maximum displacement (blue: ≤1 µm; red: >1 µm).

Video 8. **Vimentin-SunTag trajectories align with MTs.** Cells co-express MT end-binding protein EB3 (magenta) and sparsely labeled vimentin-SunTag (green). The trajectories of vimentin-SunTag particles align with EB3 comets, marking the MT tracks. A zoomed-in view of the white-boxed perinuclear region is included.

Video 9. **Fly-through of a perinuclear FIB-SEM volume containing a VIF bundle.** The first video begins by indicating the position of the subvolume containing a VIF bundle relative to the nuclear envelope. Next, a video fly-through of the subvolume is played. For enhanced clarity, we applied a 20-slice rolling maximum intensity filter to the stack, such that each frame of the fly-through is a 40-nm-thick projection. Scale = 20 nm.

Video 10. **3D reconstruction of VIFs identified and tracked from the perinuclear FIB-SEM volume indicated in** Fig. 7 A**.** Filaments are assigned a random color and progressively revealed to more clearly reveal the VIF network organization.

Video 11. **3D reconstruction of perinuclear VIFs color-coded by average relative orientation.** Blue indicates filaments co-oriented with their neighbors (<20° relative orientation), and orange indicates filaments that are not aligned with neighbors (>20° relative orientation).

Video 12. **3D reconstruction of the perinuclear VIFs (blue) and MTs (white) reconstructed from the FIB-SEM volume.**

Video 13. **3D reconstruction comparing both perinuclear and peripheral reconstructions: VIFs (blue) and MTs (gray).**